

**REPORT DOCUMENTATION PAGE**Form Approved  
OMB No. 0704-0188

Public reporting burden for this collection of information is estimated to average 1 hour per response, including the time for reviewing instructions, searching data sources, gathering and maintaining the data needed, and completing and reviewing the collection of information. Send comments regarding this burden estimate or any other aspect of this collection of information, including suggestions for reducing this burden to Washington Headquarters Service, Directorate for Information Operations and Reports, 1215 Jefferson Davis Highway, Suite 1204, Arlington, VA 22202-4302, and to the Office of Management and Budget, Paperwork Reduction Project (0704-0188) Washington, DC 20503.

**PLEASE DO NOT RETURN YOUR FORM TO THE ABOVE ADDRESS.**

<b>1. REPORT DATE (DD-MM-YYYY)</b> 10 - 08 - 2000		<b>2. REPORT TYPE</b> Final Report		<b>3. DATES COVERED (From - To)</b> 01 - 06 - 1999 -- 31 - 5 - 2000	
<b>4. TITLE AND SUBTITLE</b>  Application of Resonant Ultrasound Spectroscopy to Inhomogeneous Materials				<b>5a. CONTRACT NUMBER</b>	
				<b>5b. GRANT NUMBER</b> N00014-99-1-0708	
				<b>5c. PROGRAM ELEMENT NUMBER</b> PE 61153N	
<b>6. AUTHOR(S)</b>  McCall, Katherine R.				<b>5d. PROJECT NUMBER</b>	
				<b>5e. TASK NUMBER</b>	
				<b>5f. WORK UNIT NUMBER</b>	
<b>7. PERFORMING ORGANIZATION NAME(S) AND ADDRESS(ES)</b>  Department of Physics University of Nevada, Reno Reno, NV 89557				<b>8. PERFORMING ORGANIZATION REPORT NUMBER</b>	
<b>9. SPONSORING/MONITORING AGENCY NAME(S) AND ADDRESS(ES)</b>  Office of Naval Research 800 North Quincy St. Arlington, VA 22217-5660				<b>10. SPONSOR/MONITOR'S ACRONYM(S)</b>  ONR	
				<b>11. SPONSORING/MONITORING AGENCY REPORT NUMBER</b>	
<b>12. DISTRIBUTION AVAILABILITY STATEMENT</b>  Approved for public release; distribution is Unlimited.					
<b>13. SUPPLEMENTARY NOTES</b> Report includes Master's Thesis, Determination of Elastic Moduli of Rock Samples Using Resonant Ultrasound Spectroscopy, by TJ Ulrich, Department of Physics, University of Nevada, Reno, December 2000.					
<b>14. ABSTRACT</b> Resonant Ultrasound Spectroscopy (RUS) has been used successfully to determine the elastic properties of single crystal and homogeneous materials. We have attempted to answer the following question. Under what conditions is RUS a useful tool for determining the moduli of macroscopic, inhomogeneous samples. We concentrated on identifying a sample geometry that will maximize success with RUS. The work consisted of numerical modeling of sample resonances under varying conditions, and empirical testing of rock samples. Numerical modeling and empirical testing indicate that RUS is a viable technique for characterizing the average isotropic elastic moduli of inhomogeneous materials, although larger RMS errors can be expected than for single crystal materials. Success with RUS can be optimized by ensuring that the sample size is large compared to the scale of inhomogeneity, and by using a high aspect ratio parallelepiped sample.					
<b>15. SUBJECT TERMS</b>  elasticity, modulus, resonant ultrasound spectroscopy (RUS), inhomogeneity					
<b>16. SECURITY CLASSIFICATION OF:</b>			<b>17. LIMITATION OF ABSTRACT</b>	<b>18. NUMBER OF PAGES</b>	<b>19a. NAME OF RESPONSIBLE PERSON</b>
a. REPORT	b. ABSTRACT	c. THIS PAGE			<b>19b. TELEPHONE NUMBER (Include area code)</b>
U	U	U	UU	77	

# ONR 331/99/0251 FINAL REPORT

## Application of Resonant Ultrasound Spectroscopy to Inhomogeneous Materials

**Katherine R. McCall**

Dept. of Physics / 220  
University of Nevada  
Reno, NV 89557  
Telephone: 775-784-4991  
Fax: 775-784-1398  
Email: mccall@physics.unr.edu

**Grant #:** N00014-99-1-0708

**Grant Period:** 6/1/99 – 5/31/00

**ONR Program Officer:** Logan Hargrove

### Summary of Objectives and Approach:

Resonant Ultrasound Spectroscopy (RUS) has been used successfully to determine the elastic properties of single crystals and homogeneous materials. Our objective was to develop RUS to measure the average elastic properties of inhomogeneous materials, such as composites, concrete, and rocks. Our goal was to proscribe the conditions necessary for the successful use of RUS on inhomogeneous materials by studying the effects of size, shape, aspect ratio, and sample Q on the accuracy of RUS measurements. We focused on rock samples, believing that the strategy for establishing the applicability of RUS to rocks should generalize to other inhomogeneous materials. Rocks are consolidated materials, not easily machined, often anisotropic, and having very low quality factor, Q (or high attenuation).

We have attempted to answer the following question. Under what conditions is RUS a useful tool for determining the moduli of macroscopic (a few centimeters on a side), inhomogeneous samples? We concentrated on identifying a sample geometry that will maximize success with RUS. The work consisted of numerical modeling of sample resonances under varying conditions, and empirical testing of rock samples. Numerical modeling was based on the *Visscher et al.* [1991] variational technique, and standard perturbation techniques. Some software was developed at UNR, and some was provided by Dynamic Resonance Systems (DRS), a commercial provider of RUS measurement systems. Empirical testing was performed using a DRS system. The experimental sample shapes are rectangular parallelepipeds.

20000828 106

### Summary of Major Findings:

1. The RUS analysis technique assumes sample homogeneity. By a back-of-the-envelope argument, we claim that inhomogeneous samples will look homogeneous to RUS if the scale of the inhomogeneity is no more than  $1/5$  the smallest sample dimension. Thus average moduli can be accurately determined when the scale of sample inhomogeneity is small compared to the sample scale. Empirical testing on inhomogeneous granite samples of various sizes confirmed this concept.
2. The RUS analysis technique assumes a perfect parallelepiped sample. Using perturbation theory, we argue that for inhomogeneous samples, a nick in a corner of the sample, or two sample sides that are not perfectly parallel, will contribute negligibly to error in the measured moduli. Empirical results from crudely cut samples and samples cut precisely are essentially indistinguishable for the same rock type. Small sample shape imperfections did not cause large errors in fits for moduli.
3. Inhomogeneous samples have high attenuation, or low quality factor  $Q$ . Low  $Q$  causes resonance peaks to be short and broad. This means that resonance peaks may overlap, and may be difficult to pick out from background noise (especially as the frequency increases). To maximize the information gained from a minimum number of peaks, we modified sample aspect ratio. We modeled the spread in the first 14 resonance frequencies as a function of aspect ratio, and the contribution of the two isotropic moduli to the first resonances as a function of aspect ratio. In both cases, we found that optimum results can be obtained with sample aspect ratios of  $4/1$  (largest to smallest side). Empirical testing of black gabbro samples with varying aspect ratios, show that the error in the fits for moduli decreases as the aspect ratio is increased.
4. In theory, the RUS technique should be capable of identifying anisotropy in an experimental sample. In practice, inhomogeneity and compensations made to deal with inhomogeneity may mask clues that a sample is anisotropic. In other words, if we assume isotropy for an anisotropic sample, the RUS fitting errors should be large and obvious for a perfect sample, but may not be for inhomogeneous samples. We modeled the error induced in an isotropic fit, as a function of the strength of hexagonal anisotropy. We conclude that anisotropy will be very difficult to detect in high aspect ratio samples. In contrast, anisotropy in symmetric samples will cause degenerate resonances to split, and should be clearly distinguishable. However, low  $Q$  may cause these split peaks to overlap, and thus make the distinction impossible.

### Summary of Conclusions:

Numerical modeling and empirical testing indicate that RUS is a viable technique for characterizing the average isotropic elastic moduli of inhomogeneous materials, although larger RMS errors can be expected than for single crystal materials. Success with RUS can be optimized by ensuring that the sample size is large compared to the scale of inhomogeneity, and by using a high aspect ratio parallelepiped sample (ratio of largest side to smallest side approximately 4). Hexagonal anisotropy and lower symmetries may be difficult to detect, and even harder to quantify, except for very low attenuation materials.

**Detailed Report:**

See attached Master's Thesis, *Determination of Elastic Moduli of Rock Samples Using Resonant Ultrasound Spectroscopy*, by TJ Ulrich, Department of Physics, University of Nevada, Reno, December 2000.

**Navy Relevance:**

The development of RUS as a tool to understand thermoacoustic properties of crystalline materials is supported primarily by the Physical Acoustics Program at ONR. Our goal is to develop RUS as a tool to understand the elastic and acoustic properties of materials that constitute physical infrastructure, such as concrete, rock, laminates, and polymer composites. This corresponds to ONR's Physical Acoustics Program objective of measuring and correlating physical properties of materials using acoustic methods.

**Journal Publications:**

- Determination of elastic moduli of rock samples using resonant ultrasound spectroscopy I:  
Isotropic samples, TJ Ulrich, K. R. McCall, and R. A. Guyer, in preparation for J. Acoust. Soc. Am.
- Determination of elastic moduli of rock samples using resonant ultrasound spectroscopy II:  
Anisotropic samples, TJ Ulrich, K. R. McCall, and R. A. Guyer, in preparation for J. Acoust. Soc. Am.

**Technical Reports:**

- Determination of elastic moduli of rock samples using resonant ultrasound spectroscopy,  
Master's Thesis by TJ Ulrich, Department of Physics, University of Nevada, Reno,  
December 2000.

**Presentations:**

- RUS on rocks, K. R. McCall, Resonance Meeting, National Center for Physical Acoustics,  
Oxford, MS, May 30 – June 2, 1999.
- Application of resonant ultrasound spectroscopy (RUS) to determine the elastic properties of  
rock samples, TJ Ulrich, K. R. McCall, P. A. Johnson, T. W. Darling, and A. Migliori, 4<sup>th</sup>  
International Workshop on Nonlinear Mesoscopic Elasticity, Los Alamos, NM, July 19 – 23,  
1999.
- Resonant ultrasound spectroscopy on rocks, I. B. Santos, Fall 1999 Zone 18 Meeting of the  
Society of Physics Students, California Lutheran College, Thousand Oaks, CA, October 30,  
1999.
- Optimizing success with resonant ultrasound spectroscopy (RUS) on rock samples, TJ Ulrich, I.  
B. Santos, and K. R. McCall, Fall 1999 Meeting of the American Geophysical Union, San  
Francisco, CA, December 13 – 17, 1999.
- What is RUS on rocks?, I. B. Santos, Spring 2000 Zone 18 meeting of the Society of Physics  
Students, Stanford University, Stanford, CA, April 8, 2000.

RUS and rocks: Aspect ratio and anisotropy, K. R. McCall, 5<sup>th</sup> International Workshop on Nonlinear Mesoscopic Elasticity, Santa Margherita, Italy, July 5 – 8, 2000.  
Resonant ultrasound spectroscopy (RUS) on rocks, I. B. Santos, International Congress of Physics Students, Zadar, Croatia, August 5 – 11, 2000.

### **Students Supported:**

TJ Ulrich, graduate research assistant. Completed a Physics MS (December 2000). Continuing in the PhD program.  
Izabela Santos, undergraduate student worker. Senior thesis in progress.

### **Other Sponsored Awards During Grant Period:**

Resonant mode inversion technique for rock characterization II (co-PI Paul Johnson, LANL), Institute for Geophysics and Planetary Physics, Los Alamos National Laboratory, 10/1/98 -- 9/30/99, \$25,000 awarded.  
Neutron spectroscopy of earth materials (co-PI Juergen Eckert, LANL), Institute for Geophysics and Planetary Physics, Los Alamos National Laboratory, 10/1/99 -- 9/30/01, \$44,000 awarded.  
Ultrasonic determination of moduli in earth materials (co-PI Paul Johnson, LANL), Institute for Geophysics and Planetary Physics, Los Alamos National Laboratory, 10/1/99 -- 9/30/01, \$44,000 awarded.  
A computational laboratory for outreach programs, Modern Physics (PHYS 421), and Advanced Laboratory Techniques (PHYS 423) (co-PI Roberto Mancini, UNR), Excellence in Teaching Program, University of Nevada, Reno, 1/1/99 -- 6/30/99, \$500 awarded.  
Resonant mode inversion technique for rock characterization, Junior Faculty Research Award, University of Nevada, Reno, 7/1/98 -- 12/31/99, \$10,000 awarded.

### **Continuing Program:**

During the past year, we performed a feasibility study showing that with the proper choice of sample geometry, RUS can be used to measure elastic moduli of inhomogeneous materials quickly and accurately. The RUS measurement system can be used to monitor the elastic state of an inhomogeneous sample. In the next year, we have two goals: 1) to broaden the range of inhomogeneous samples to which RUS can be applied (we are particularly interested in cylindrical samples), and 2) to develop RUS as a tool to probe the response of rocks and concrete to quasistatic and dynamic perturbations (we are particularly interested in dependence on temperature and vapor pressure). An experimental system will be developed to allow control of temperature (first) and vapor pressure (second), and a series of experiments that follow the evolution of the elastic state in response to these variables will be performed. We believe the outcome of these experiments will provide important new insights regarding the microscopic mechanism causing the nonlinear elastic behavior displayed by rocks and concrete.

## Report Distribution:

Logan E. Hargrove  
Program Officer, ONR 331  
Office of Naval Research  
Ballston Centre Tower One  
800 North Quincy St.  
Arlington, VA 22217-5660

Director, Naval Research Laboratory  
Attn: Code 5227  
4555 Overlook Dr.  
Washington, DC 20375-5326

Defense Technical Information Center  
8725 John J. Kingman Rd.  
STE 0944  
Ft. Belvoir, VA 22060-6218

Orson L. Anderson  
Inst. for Geophysics and Planetary Physics  
University of California at Los Angeles  
4851 Geology Building  
Los Angeles, CA 90095-1567

Timothy W. Darling  
MS K764  
Los Alamos National Laboratory  
Los Alamos, NM 87545

Robert Gose  
Dynamic Resonance Systems Inc  
225 Lane 13  
Powell, WY 82435

Robert A. Guyer  
Department of Physics  
Hasbrouck Laboratory  
University of Massachusetts  
Amherst, MA 01003

Donald G. Isaak  
Inst. for Geophysics and Planetary Physics  
University of California at Los Angeles  
4851 Geology Building  
Los Angeles, CA 90095-1567

Veerle Keppens  
National Center for Physical Acoustics  
University of Mississippi  
PO Box 1848  
University, MS 38677

Julian D. Maynard  
Department of Physics  
Pennsylvania State University  
University Park, PA 16802

Albert Migliori  
MS K764  
Los Alamos National Laboratory  
Los Alamos, NM 87545

James A. TenCate  
MS D443  
Los Alamos National Laboratory  
Los Alamos, NM 87545

University of Nevada, Reno

**Determination of Elastic Moduli  
of Rock Samples  
Using Resonant Ultrasound Spectroscopy**

A thesis submitted in partial fulfillment of the  
requirements for the degree of  
Master of Science in Physics

by

Timothy James Ulrich II

Dr. Katherine R. McCall, Thesis Advisor

December, 2000

UNIVERSITY  
OF NEVADA  
RENO

THE GRADUATE SCHOOL

We recommend that the thesis  
prepared under our supervision by

**TIMOTHY JAMES ULRICH II**

entitled

**Determination of Elastic Moduli of Rock Samples  
Using Resonant Ultrasound Spectroscopy**

be accepted in partial fulfillment of the  
requirements for the degree of

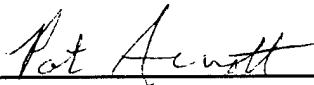
**MASTER OF SCIENCE**



Katherine McCall, Ph.D., Thesis Advisor



Paul Neill, Ph.D., Committee Member



W. Patrick Arnott, Ph.D., At-Large Member

Kenneth W. Hunter, Jr., Sc.D., Dean, Graduate School

December, 2000



## ACKNOWLEDGMENTS

First I would like to thank my advisor Dr. Katherine McCall and Dr. Robert Guyer for the time they took to explain this world to me, and for the patience to re-explain it again and again. I would also like to thank my parents for instilling in me a desire to always know more, and for supporting me throughout this process.

This project would not have been possible without the financial assistance that I received through a grant from the Office of Naval Research (ONR), Physical Acoustics Program. Additional support was provided by the Institute of Geophysics and Planetary Physics (IGPP), at Los Alamos National Laboratory (LANL). Special thanks to ONR program officer Logan Hargrove, and IGPP/LANL director Chick Keller.

Equipment was graciously provided by Paul Johnson of EES-4, who also, along with Jim Albright, provided summer research opportunities using RUS in the EES-4 research group at Los Alamos National Laboratory. In the past two years I have had the pleasure of working with Tim Darling and Albert Migliori, to whom I owe many thanks for all of their advice and assistance.

Here at the University of Nevada, Reno, I would like to thank the physics department machine shop staff for their help in constructing a sample stage; Dr. Richard Schweickert and the School of Mines for providing access to sample preparation equipment; and finally to Dr. Paul Neill and Dr. Pat Arnott for taking the time to read this thesis, despite all of the delays. My thanks also go out to Izabela Santos, an undergraduate physics student, for her assistance over the past year.

## ABSTRACT

Resonant Ultrasound Spectroscopy (RUS) is a method whereby the elastic tensor of a sample is extracted from measured resonance frequencies. RUS has been used successfully to determine the elastic properties of single crystals and homogeneous samples. In this thesis, I study the applicability of RUS to macroscopic samples of inhomogeneous materials, specifically rock. I have paid particular attention to several issues: appropriate scale of inhomogeneity, sample shape imprecision, effects of low  $Q$ , extraction of sufficient information on multiple moduli, and recognition of anisotropy. Using modeling and empirical testing, I have established bounds on the applicability of RUS to inhomogeneous materials.

“Six months in the lab can save you a day in the library.”

– old adage

# Table of Contents

<b>1</b>	<b>INTRODUCTION</b>	<b>2</b>
<b>2</b>	<b>VARIATIONAL CALCULATION OF ELASTIC RESONANCES AND LEVENBERG-MARQUARDT INVERSION</b>	<b>6</b>
2.1	Variational Calculation of Elastic Resonances in One Dimension . . .	7
2.2	Three Dimensional Model . . . . .	13
2.3	Levenberg-Marquardt Minimization . . . . .	17
<b>3</b>	<b>MODELING AND EXPERIMENTAL DEVELOPMENT</b>	<b>20</b>
3.1	Free boundaries . . . . .	22
3.2	Inhomogeneity . . . . .	23
3.3	Sample geometry, the figure of the sample . . . . .	24
3.4	Distinct resonance peaks . . . . .	25
3.5	$c_{11}$ dependence . . . . .	26
3.6	Anisotropy . . . . .	30
<b>4</b>	<b>EXPERIMENTAL RESULTS AND CONCLUSIONS</b>	<b>37</b>

4.1 Results . . . . .	37
4.2 Conclusions . . . . .	41
<b>A PERTURBATION THEORY</b>	<b>43</b>
<b>B CASE STUDY</b>	<b>46</b>
<b>REFERENCES</b>	<b>61</b>

# List of Figures

2.1	Example of a vibrating string with free ends. . . . .	9
2.2	Comparison of one dimensional mode shapes. . . . .	12
2.3	Examples of three dimensional mode shapes . . . . .	14
2.4	Comparison of numerical method for number of frequencies predicted by $N = 10$ and $N = 12$ . . . . .	16
3.1	Block diagram of experimental set-up . . . . .	21
3.2	Frequency shift as a function of the perturbation placement. . . . .	25
3.3	Resonance frequencies as a function of aspect ratio. . . . .	27
3.4	$c_{11}$ dependence as a function of aspect ratio. . . . .	29
3.5	Frequency error vs. $\varepsilon$ for $c/a = -4, -2, 1, 2, 3, 4$ . . . . .	33
3.6	Quality of fit for $c/a=4$ , hexagonal symmetry. . . . .	34
3.7	Quality of fit for $c/a=2$ , hexagonal symmetry. . . . .	35
3.8	Quality of fit for $c/a=4$ , fixed $\varepsilon$ , varying number of frequencies fit. . .	35
4.1	Pictorial representation of sample set 1. . . . .	39
B.1	Example of a spectrum for a stainless steel. . . . .	47

B.2	Example of a spectrum for Berea sandstone. . . . .	48
B.3	Input file for sample BG-4, forward calculation. . . . .	50
B.4	Initial scan of sample BG-4. . . . .	51
B.5	Scan of region A for sample BG-4. . . . .	52
B.6	Artifact scan of sample BG-4, region E. . . . .	53
B.7	Sample BG-4, scan of region B. . . . .	54
B.8	Sample BG-4, scan of region C. . . . .	55
B.9	Sample BG-4, scan of region D. . . . .	56
B.10	Sample BG-4, scan of region F. . . . .	57
B.11	Sample BG-4, scan of region G. . . . .	58
B.12	Input file for sample BG-4. . . . .	58
B.13	Final output file for sample BG-4. . . . .	60

## List of Tables

1.1	Relationships for engineering elastic constants in isotropic materials .	5
4.1	Sample Set 1 . . . . .	38
4.2	Sample Set 2 . . . . .	39



# Chapter 1

## INTRODUCTION

Resonant ultrasound spectroscopy (RUS) is a highly sensitive technique for determining the elastic tensor and related properties of single crystal samples [1]. The first ten or more resonance frequencies of a sample with free boundaries are measured. These resonance frequencies are the input to an iterative inversion algorithm that finds the best match between the data and a set of resonance frequencies generated from a model. The variational parameters in the inversion are the components of the elastic tensor describing the sample. Thus RUS is a method whereby the elastic tensor of a sample is extracted from measured resonance frequencies. For example, RUS has been used to determine the elastic tensor and crystallographic orientation of tantalum [2], to measure the elastic properties and infer thermodynamic properties of CaO at temperatures representative of the earth's interior [3], and to study the elastic constants, microstructure, and superconducting phase transition in  $\text{La}_{2-x}\text{Sr}_x\text{CuO}_4$  [4]. The elastic tensor of single crystals and minerals reflects the angstrom scale structure

of these systems. From knowledge of the elastic tensor, the symmetry of a crystal and features of the phonon and electron spectra can be deduced. When RUS is conducted in a temperature reservoir that can be controlled, it is possible to develop a complete thermodynamic description of the sample.

The success of RUS derives from the sensitivity of the resonant modes of a system to the elastic structure of the system [5]. The elastic structure affecting resonance frequencies has three components: the geometry of the sample; the homogeneity of the sample; and the elastic tensor of the sample, including symmetry and orientation. Given a perfectly homogeneous sample with a precise geometry, the elastic tensor can be derived to a very high degree of accuracy.

In this paper, we explore the limits of applicability of RUS to macroscopic, inhomogeneous samples of rock. Rocks are consolidated materials, typically assembled from aggregates of mesoscopic sized pieces of atomically uniform materials. They are not easily machined to precise shapes. Their microscopic symmetry is homogenized by the process of their macroscopic assembly. However, they may have macroscopic symmetry of great importance. My goal is to proscribe the conditions necessary for the successful use of RUS on inhomogeneous materials. These conditions include constraints on sample preparation and constraints on the body of reasonable questions that can be answered with RUS.

Historically, the elastic moduli of macroscopic inhomogeneous materials have been measured using mechanical testing [6] or ultrasonic time-of-flight techniques [7]. Mechanical testing, wherein the stress-strain relationship is measured between am-

bient conditions and failure, is a widely accepted method for measuring material strength and toughness. A modulus is determined from the stress-strain slope at low strain. The greatest disadvantage to using mechanical testing to determine linear elastic moduli is that the sample is destroyed or altered as a result of the test. Thus results cannot be confirmed for a given sample, and only one elastic constant can be determined for each sample. Another disadvantage is that mechanical tests are inherently high amplitude tests. Our primary interest is in dynamic moduli that are directly related to acoustic velocities. In general, dynamic moduli measured by time-of-flight techniques are higher than moduli inferred from mechanical testing.

Time-of-flight determinations of elastic constants are actually acoustic velocity measurements. The time delay  $t$  of an ultrasonic pulse across the sample is measured. Given the length  $l$  and density  $\rho$  of the sample, the wave velocities and elastic constants can be determined from  $v = l/t$ ,  $c_{11} = \rho v_c^2$ , and  $c_{44} = \rho v_s^2$ , where  $v_c$  and  $v_s$  are the compressional and shear wave velocities (Table 1.1 provides a relationship between  $c_{11}$ ,  $c_{44}$  and the standard engineering elastic constants). This technique is path dependent and therefore requires multiple measurements in different locations and directions to determine an average velocity if the material is inhomogeneous. To determine both compressional and shear velocities, transducers that produce purely compressional and purely shear plane waves are desirable. Finally, the transducers must be bonded to the sample reproducibly for all measurements.

Resonant ultrasound spectroscopy is a potential alternative technique for determining elastic moduli of inhomogeneous materials. Typically, a rectangular par-

Table 1.1: Relationships for engineering elastic constants in isotropic materials

	Bulk	Young's	Shear	Lamé	Compressional
	B	E	G, $c_{44}$	$\lambda$	$c_{11}$
B, E	-	-	$\frac{3BE}{9B-E}$	$3B\frac{3B-E}{9B-E}$	$3B\frac{3B+E}{9B-E}$
B, G	-	$\frac{9BG}{3B+G}$	-	$B - \frac{2}{3}G$	$B + \frac{2}{3}G$
E, G	$\frac{GE}{3(3G-E)}$	-	-	$G\frac{E-2G}{3G-E}$	$G\frac{4G-E}{3G-E}$
$\lambda, \mu$	$\lambda + \frac{2}{3}\mu$	$\frac{\mu(3\lambda+2\mu)}{\lambda+\mu}$	$\mu$	-	$\lambda + 2\mu$
$c_{11}, c_{44}$	$c_{11} - \frac{4}{3}c_{44}$	$\frac{3c_{44}(c_{11}-\frac{4}{3}c_{44})}{c_{11}-c_{44}}$	-	$c_{11} - 2c_{44}$	-

allelepiped sample is placed between two piezoelectric transducers, a source and a detector. The sample is driven at constant voltage as the frequency is swept through multiple resonances. The measured resonance frequencies are the input to an iterative inversion algorithm that finds the best match between the data and a set of resonances generated from a model. The experimental component of RUS is straightforward. The analysis component is sophisticated, but can be performed more and more rapidly as computational power increases. Chapter 2 will examine the numerical process involved in the RUS analysis. In Chap. 3, several issues pertaining to using RUS on inhomogeneous samples are discussed. In most cases, numerical modeling was used to explore ways to optimize experimental chances for success. In Chap. 4, the results of RUS experiments on a variety of samples are displayed and discussed as well as a summary of our findings, describing the bounds on RUS applicability to inhomogeneous materials found empirically and through modeling.

## Chapter 2

# VARIATIONAL CALCULATION OF ELASTIC RESONANCES AND LEVENBERG-MARQUARDT INVERSION

The Resonant Ultrasound Spectroscopy (RUS) technique has two components: the experiment to collect resonance frequencies, and the analysis to extract the elastic moduli. The bulk of this thesis is a description of the experimental application of RUS, and the numerical modeling used to optimize the experimental results. In this chapter the mathematical and theoretical basis of the analysis component will be described for two physical systems: a one dimensional string, and a three dimensional elastic solid. The example in one dimension is used to illustrate the principles of the three dimensional calculation.

While elastic resonances in one dimension are relatively easy to calculate ana-

lytically, the resonances of an arbitrary three dimensional object with arbitrary symmetry are extremely difficult to calculate. The analysis built into the RUS technique uses a variational scheme to calculate approximate resonances [8]. This approximation technique decreases the calculation time considerably and can be applied to arbitrary shape and symmetry in a straightforward manner. In addition, extremely accurate results can be obtained when an appropriate number of basis functions is employed.

## 2.1 Variational Calculation of Elastic Resonances in One Dimension

Hamilton's variational principle is used to calculate the resonance frequencies of an arbitrary body. We illustrate this calculation in one dimension. The Lagrangian of a string of length  $l$  is

$$L = \int_l (T - U) dx , \quad (2.1)$$

where  $T$  is the kinetic energy and  $U$  is the potential energy per unit length of the string. In frequency space

$$T = \frac{1}{2} \rho \omega^2 u^2 , \quad (2.2)$$

and

$$U = \frac{1}{2} \tau \left( \frac{\partial u}{\partial x} \right)^2 , \quad (2.3)$$

where  $\rho$  is the mass density,  $\tau$  is the string tension,  $\omega$  is the frequency of motion, and  $u$  is the transverse displacement at  $x$ . Thus the Lagrangian is

$$L = \int_l \left[ \frac{1}{2} \rho \omega^2 u^2 - \frac{1}{2} \tau \left( \frac{\partial u}{\partial x} \right)^2 \right] dx . \quad (2.4)$$

Varying our original Lagrangian by  $\delta L$ , Eq. (2.4) becomes

$$L + \delta L = \int_l \left[ \frac{1}{2} \rho \omega^2 (u + \delta u)^2 - \frac{1}{2} \tau \left( \frac{\partial(u + \delta u)}{\partial x} \right)^2 \right] dx . \quad (2.5)$$

To first order in the variational parameter  $\delta u$ ,

$$\delta L = \int_l \left[ \rho \omega^2 u \delta u - \tau \left( \frac{\partial u}{\partial x} \right) \left( \frac{\partial \delta u}{\partial x} \right) \right] dx . \quad (2.6)$$

Integrating by parts we find

$$\delta L = \int_l dx \left[ \rho \omega^2 u - \frac{\partial}{\partial x} \left( \tau \frac{\partial u}{\partial x} \right) \right] \delta u - \tau \left( \frac{\partial u}{\partial x} \right) \delta u \Big|_0^l . \quad (2.7)$$

To minimize the Lagrangian we set  $\delta L = 0$ . For arbitrary  $\delta u$ , Hamilton's principle is satisfied when two conditions are met:

**First Condition:**

$$\tau \frac{\partial u}{\partial x} \Big|_0^l = 0 \quad (2.8)$$

**Second Condition:**

$$\rho \omega^2 u + \tau \frac{\partial^2 u}{\partial x^2} = 0 \quad (2.9)$$

The first condition is equivalent to the free boundary condition at each end of the string. The second is the one dimensional wave equation. Thus the displacement function  $u(x)$  that minimizes the Lagrangian, solves the elastic wave equation for a string with free ends, as illustrated in Fig. 2.1.

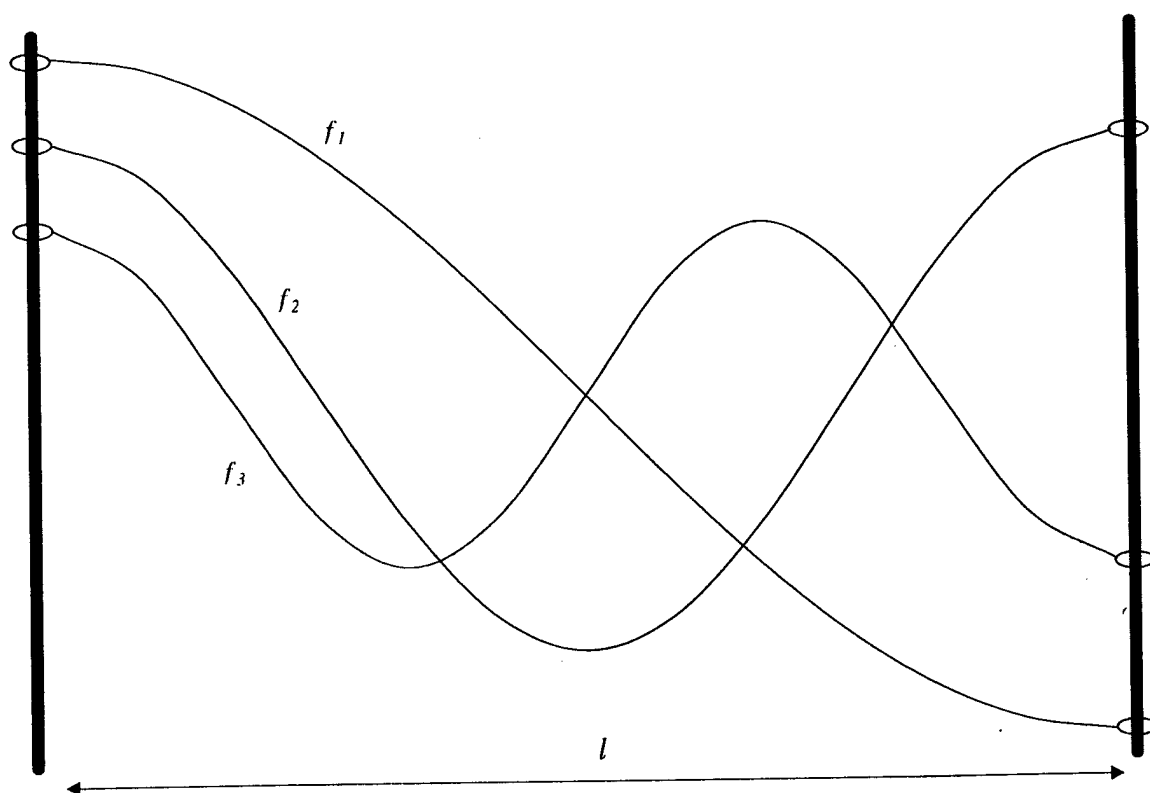


Figure 2.1: Example of string with free ends. The ends are free to slide along the guide bars without friction.



Applying the results of the previous paragraph, we choose a convenient form for  $u(x)$  that includes variational parameters that will allow us to minimize  $L$ . Following Visscher et al. [9] we choose  $u(x)$  to be a polynomial,

$$u(x) = \sum_{n=0}^N a_n x^n. \quad (2.10)$$

Substituting  $u(x)$  in Eq. (2.4) we have

$$L = \int_l dx \left[ \frac{1}{2} \rho \omega^2 \sum_{n=0}^N a_n x^n \sum_{m=0}^N a_m x^m - \frac{1}{2} \tau \sum_{n=0}^N a_n \frac{\partial x^n}{\partial x} \sum_{m=0}^N a_m \frac{\partial x^m}{\partial x} \right]. \quad (2.11)$$

Simplifying,

$$L = \frac{1}{2} \omega^2 \sum_{n,m=0}^N a_n a_m E_{nm} - \frac{1}{2} \sum_{n,m=0}^N a_n a_m n m \Gamma_{nm}, \quad (2.12)$$

where

$$E_{nm} = \frac{\rho l^{n+m+1}}{n+m+1}, \quad (2.13)$$

and

$$\Gamma_{nm} = \begin{cases} n m \tau \frac{l^{n+m-1}}{n+m-1} & \text{for } n \& m \neq 0 \\ 0 & \text{for } n \text{ or } m = 0 \end{cases}. \quad (2.14)$$

To minimize the Lagrangian, we set  $\partial L / \partial a_i = 0$ . This leads to  $N$  linear equations that can be expressed in matrix form,

$$(\omega^2 \mathbf{E} - \mathbf{\Gamma}) \mathbf{a} = 0. \quad (2.15)$$

We now have an eigenvector/eigenvalue problem. Setting the determinant  $|\omega^2 \mathbf{E} - \mathbf{\Gamma}| = 0$ , we find  $N+1$  values of  $\omega^2$ . For each frequency eigenvalue  $\omega^2$ , there is an eigenvector  $\mathbf{a}$  that contains the values of the coefficients of the displacement polynomial  $u(x)$ .

As a concrete example, take  $N = 2$ . Then  $u(x) = a_0 + a_1 x + a_2 x^2$ . Let  $l = \rho = \tau = 1$  for simplicity. Then the eigenvalue/eigenvector equation reduces to

$$\omega^2 \mathbf{E} - \mathbf{\Gamma} = \begin{pmatrix} \omega^2 & \frac{1}{2}\omega^2 & \frac{1}{3}\omega^2 \\ \frac{1}{2}\omega^2 & \frac{1}{3}\omega^2 - 1 & \frac{1}{4}\omega^2 - 1 \\ \frac{1}{3}\omega^2 & \frac{1}{4}\omega^2 - 1 & \frac{1}{5}\omega^2 - \frac{4}{3} \end{pmatrix}. \quad (2.16)$$

Setting  $|\omega^2 \mathbf{E} - \mathbf{\Gamma}| = 0$ , we find the eigenvalue/eigenvector pairs:

$$\omega_0^2 = 0, \mathbf{a}_0 = \begin{pmatrix} 1 \\ 0 \\ 0 \end{pmatrix}, \quad (2.17)$$

$$\omega_1^2 = 12, \mathbf{a}_1 = \begin{pmatrix} 1 \\ -2 \\ 0 \end{pmatrix}, \quad (2.18)$$

$$\omega_2^2 = 60, \mathbf{a}_2 = \begin{pmatrix} 1 \\ -6 \\ 6 \end{pmatrix}, \quad (2.19)$$

The nontrivial eigenvalue/eigenvector pairs give us the two solutions

$$u_1(x) = 1 - 2x, \quad (2.20)$$

and

$$u_2(x) = 1 - 6x + 6x^2. \quad (2.21)$$

Comparing these numerical solutions to the analytical solutions

$$\omega_n^2 = \left(\frac{n\pi}{l}\right)^2, u_n(x) = \cos(\omega x), \quad (2.22)$$

(Fig. 2.2), we can see that the shape is not identical. As  $N$  increases, the nature of the variational technique is such that the frequencies from the variational solution converge rapidly to those of the exact solution, despite the inaccuracies in the modes

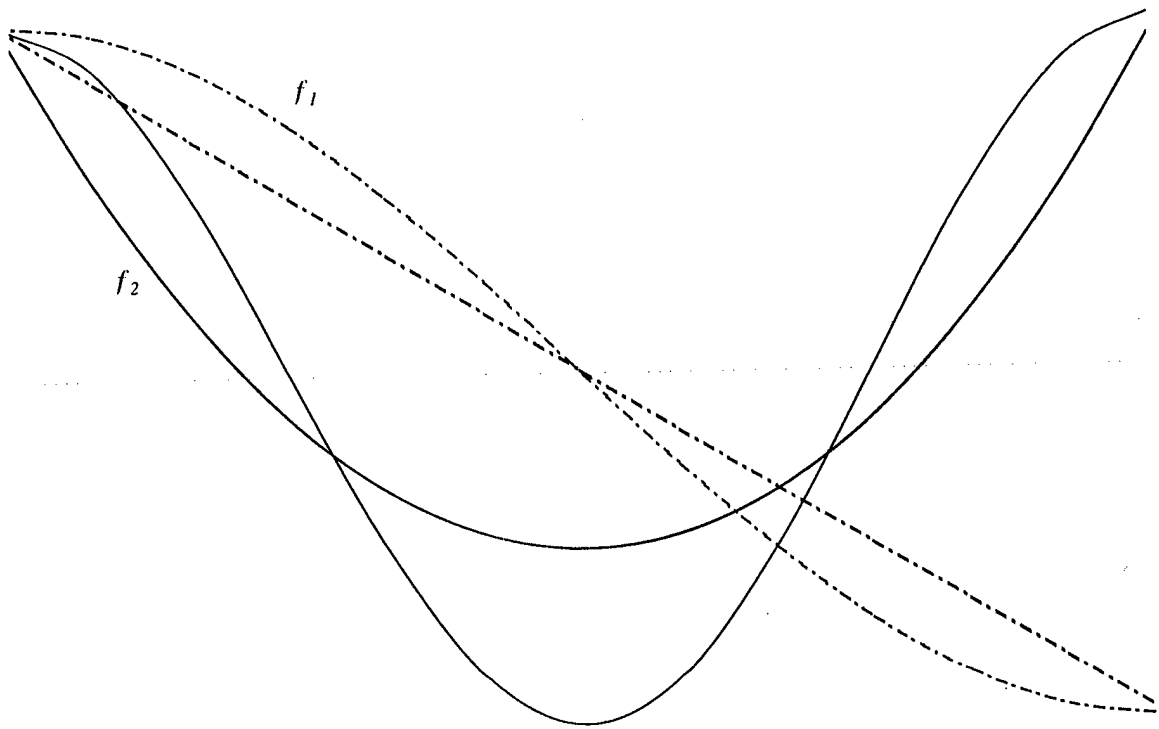


Figure 2.2: Comparison of one dimensional mode shapes. Analytical solutions in red, solutions from Visscher's algorithm ( $N = 2$ , Eqs. ( 2.20) and ( 2.21)) in blue.

shapes [10]. Notice that the first frequency,  $\omega_0^2$ , is zero. This corresponds to the translation of the string with no vibration. As an experiment only measures vibrational modes, we can neglect the translational mode. It is apparent now that assuming a polynomial solution of order  $N = 2$  is very restrictive, limiting us to  $N$  frequencies that can be calculated and compared to the experiment. Note that an  $N^{th}$  order polynomial solution for  $u(x)$  has a maximum of  $N$  nodes.

## 2.2 Three Dimensional Model

Figure 2.3 shows some exaggerated mode shapes for a parallelepiped. Comparing these to the modes shapes shown in Fig. 2.2, it is immediately obvious that the three dimensional model will be much more complicated. Hamilton's variational principle can be used to find the resonance frequencies of a 3-D elastic solid in much the same way as for the 1-D case. However, the complexity of the problem rises dramatically, especially for non-isotropic systems. Here we state the results and equations equivalent to those described in Sec. 2.1.

We choose a three dimensional polynomial for the variational solution,

$$u_i = \sum_{\lambda} a_{i\lambda} \Phi_{\lambda} , \quad (2.23)$$

where

$$\Phi_{\lambda} = x^l y^m z^n , \quad (2.24)$$

$$N \geq l + m + n , \quad (2.25)$$

and  $\lambda$  is an index to distinguish between sets of  $l, m, n$ . The Lagrangian of Eq. (2.1)

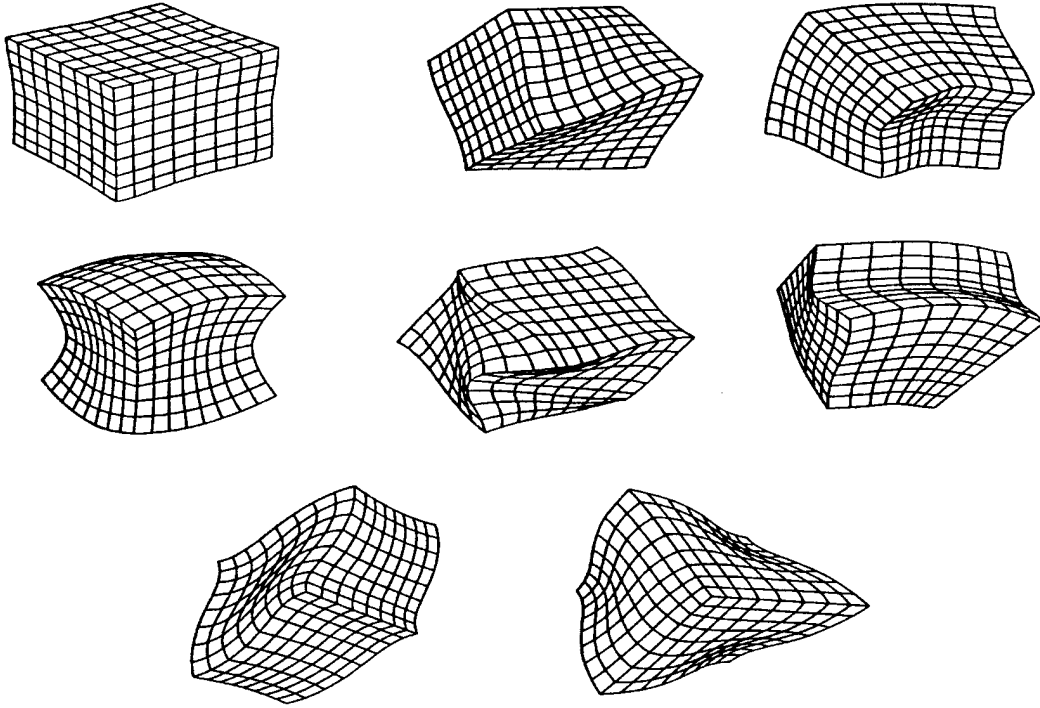


Figure 2.3: Examples of three dimensional mode shapes.

for a three dimensional system then becomes

$$L = \int_V \left[ \sum_{i,i',\lambda,\lambda'} \delta_{ii'} \rho \omega^2 a_{i\lambda} a_{i'\lambda'} \Phi_\lambda \Phi_{\lambda'} - \frac{1}{2} \sum_{i,j,k,l,\lambda,\lambda'} c_{ijkl} a_{i\lambda} a_{j'\lambda'} \frac{\partial \Phi_\lambda}{\partial x_j} \frac{\partial \Phi_{\lambda'}}{\partial x_l} \right] dV, \quad (2.26)$$

where  $c_{ijkl}$  is defined from the generalized Hooke's law [11]

$$\sigma_{ij} = c_{ijkl} \epsilon_{kl}, \quad (2.27)$$

and

$$c_{ijkl} = c_{jikl} = c_{klij} = c_{ijlk}, \quad (2.28)$$

by symmetry. Thus, only 21 of the 81 components are independent, and  $c_{ijkl}$  is commonly rewritten as a 36-component second order tensor  $c_{ij}$ . Also by symmetry,  $\sigma_{ij}$  and  $\epsilon_{kl}$  have only six independent components, and are commonly rewritten as 6-component first order tensors.

Defining

$$E_{\lambda i \lambda' i'} = \delta_{ii'} \int_V \Phi_{\lambda \rho} \Phi_{\lambda'} dV \quad (2.29)$$

and

$$\Gamma_{\lambda i \lambda' i'} = \sum_{j, j'} c_{ij i' j'} \int_V \frac{\partial \Phi_{\lambda}}{\partial x_j} \frac{\partial \Phi_{\lambda'}}{\partial x_{j'}} dV, \quad (2.30)$$

we can write the lagrangian in tensor form,

$$L = \frac{1}{2} \omega^2 \mathbf{a}^T \mathbf{E} \mathbf{a} - \frac{1}{2} \mathbf{a}^T \mathbf{\Gamma} \mathbf{a}, \quad (2.31)$$

analogous to Eq. (2.12) for the 1-D case, but more difficult to perform as  $\mathbf{a}$  is now a rank 3 tensor with  $N^3$  elements. This then leads to an eigenvalue equation

$$\omega^2 \mathbf{E} \mathbf{a} = \mathbf{\Gamma} \mathbf{a}. \quad (2.32)$$

Solving this system as  $N \rightarrow \infty$  would give an exact solution, but is analytically impossible. Thus a numerical solution must be found. To allow for a realistic computational time we have limited our numerical solution to a polynomial solution of the order  $N = 10$ .

For any nontrivial  $N$ , the diagonalization of Eq. (2.32) is performed numerically. As in the one dimensional case, the variationally determined frequencies increase in accuracy as the parameter  $N$  increases. However, the computational time and memory requirements also increase with  $N$ . We have limited the order of our three-dimensional polynomial to  $N = 10$ . Figure 2.4 [12] shows a comparison of the number of resonance frequencies that may be determined accurately for  $N = 10$  and  $N = 12$ . The sample is  $\text{SrTiO}_3$  and of cubic symmetry (3 independent elastic constants). The numerically derived frequencies are compared to the experimentally

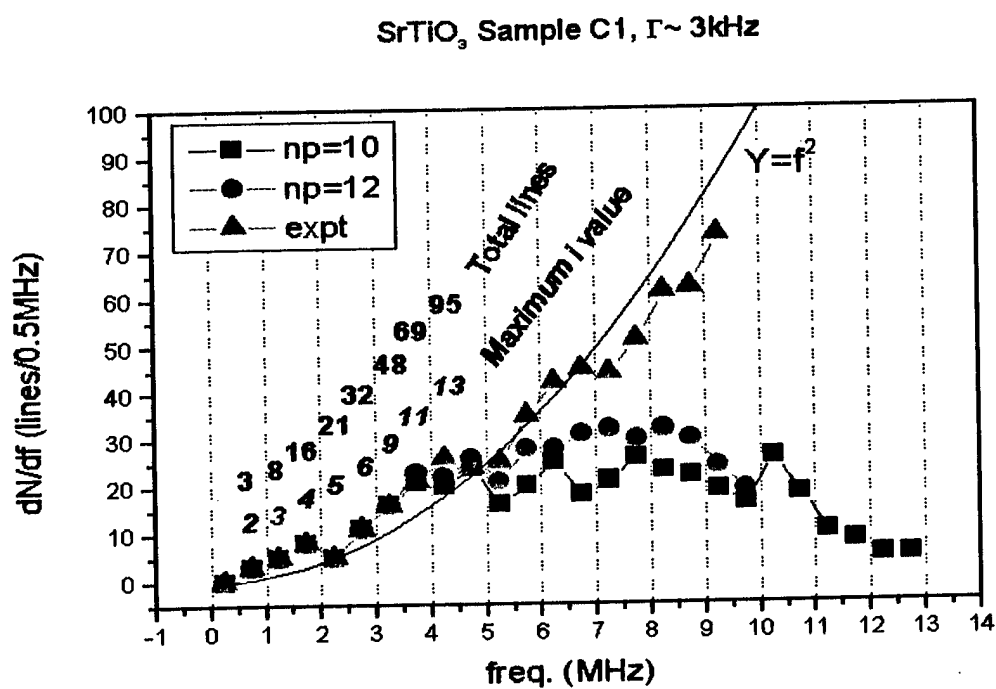


Figure 2.4: Comparison of numerical method for number of frequencies predicted by  $N = 10$  and  $N = 12$  to the actual number of observed frequencies. [12]

derived frequencies and to the standard  $f^2$  result. Note that up to 50 frequencies may be fit with the choice  $N = 10$ . Since, in general, we cannot distinguish more than 20 resonances from our rock samples, we are comfortable with  $N = 10$ .

## 2.3 Levenberg-Marquardt Minimization

In Sec. 2.2 we describe a forward calculation of resonance frequencies. After the resonance frequencies have been calculated for a given initial guess of  $c_{ijkl}$  ( $\tau$  from Sec. 2.1), the RUS inversion algorithm compares the calculated values to those measured experimentally. If the calculated frequencies do not match the experimental values, a new elastic tensor is chosen using a Levenberg-Marquardt minimization of  $\chi^2$ , where  $\chi^2$  is defined as the rms error between the calculated and measured frequencies,

$$\chi^2 = \sum_{i=1}^M [f_i^X - f_i^T]^2, \quad (2.33)$$

$M$  is the number of frequencies used for the fit,  $f_i^X$  is the  $i^{\text{th}}$  experimentally measured frequency, and  $f_i^T$  is the  $i^{\text{th}}$  calculated frequency. These three steps: calculation of resonances from an elastic tensor, comparison of calculated and experimental resonances, and a new choice of elastic tensor, are repeated until a fit is achieved. What is defined as a good match or fit will be discussed in Ch. 3. Here we will discuss some of the details of the minimization technique.

The Levenberg-Marquardt minimization technique [13] combines a steepest descents minimization with the Newtonian minimization method. This allows a rapid convergence upon the absolute minimum of the  $\chi^2$  surface. The steepest descents



method is used far from the minimum in  $\chi^2$ . The Levenberg-Marquardt algorithm switches to the Newtonian method continuously as the minimum is approached.  $\chi^2$  is a dimensionless quantity, and is looked upon throughout this thesis as a surface in  $c_{11}, c_{44}$  space. This analogy, however, does not hold as the modeled material deviates from isotropy, i.e., as more independent elastic constants are introduced.

The general procedure for using the Visscher et al [9] variational technique and the Levenberg-Marquardt method to determine elastic constants of a material is as follows:

- Guess initial values of elastic constants ( $C_{guess}$ ).
- Compute resonance frequencies for a sample characterized by ( $C_{guess}$ ) and the geometry of the experimental sample.
- Compute  $\chi^2(C_{guess}, C_{exp})$  for the model frequencies.
- Increment  $C_{guess}$  and repeat the procedure above until  $\chi^2(C_{guess}, C_{exp})$  is minimized.

In this procedure, the increment size of  $C_{guess}$  can vary, and depends on the value of  $\chi^2(C_{guess}, C_{exp})$ . This allows for a rapid and accurate convergence upon the minimum even when starting at a point far from the absolute minimum. It should be noted, however, that due to the potential complexity of the  $\chi^2$  surface, relative or false minima may exist. For this reason extreme differences in the initial guess and the absolute minimum, may cause a false minimum to be found and result in erroneous results; thus the more educated we can be when making our initial guess at the elastic

constants, the more certain we can be that we have found the absolute minimum [13].

Another important feature of the Levenberg-Marquardt method, is that it provides information about the surrounding surface of  $\chi^2$  about the minimum. That is to say, that the curvature or sharpness of the minimum is known when the minimum is found. This sharpness can differ in orders of magnitude from sample to sample, which allows us to not only find the elastic constants, but to assess the degree of certainty in our results. A very shallow minimum implies there is room for error, while a sharp minimum makes us much more confident in our results. This is an important key when evaluating the quality of our experimental results, and will be discussed more in Sec. 3.6.

## Chapter 3

# MODELING AND EXPERIMENTAL DEVELOPMENT

In this section we will apply the methods described in Chap. 2 to model and analyze experiments performed on macroscopic samples of inhomogeneous rock. The assumptions inherent in the analysis described in Chap. 2 will be discussed, as well as ways in which to maximize the success of RUS on samples whose properties do not satisfy these assumptions.

The experimental system is shown in Fig. 3.1. The sample, a rectangular parallelepiped, is held delicately between two piezoelectric transducers, one acting as the source and the other as a detector. The source is driven at constant voltage and the frequency is swept through the low-lying resonances. The measured resonance frequencies are the input to the iterative inversion algorithm discussed in Chap. 2. The algorithm finds the best match between the data (typically 10 to 20 resonance

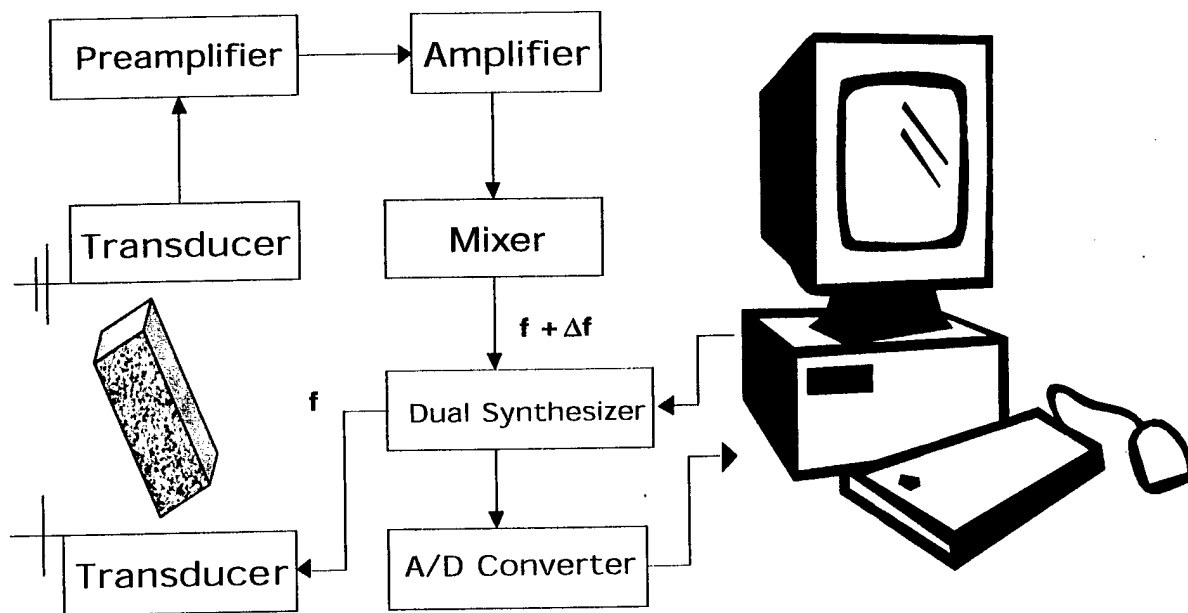


Figure 3.1: Diagram of experimental set-up. The control hardware and software are commercial packages from Dynamic Resonance Systems, Inc.

frequencies) and a set of resonances generated from a model in which the parameters are the components of the elastic tensor.

The numerical inversion is performed by software provided by Dynamic Resonance Systems (DRS), a commercial provider of RUS measurement systems, and is based on the Visscher et al. [9] variational technique. The analysis software employs a model of the resonant elastic system that (a) has free boundaries, (b) is spatially homogeneous, and (c) is a rectangular parallelepiped. Departure of a sample from these three conditions can introduce shifts in the experimental resonances, and thus will introduce error in the derived elastic moduli. Conditions (a), (b), and (c), how well our samples conform to them, and estimates of the induced error due to nonconformity are discussed below. In Appendix A we sketch a perturbation theory calculation that we use to assess the consequences of shape departures from a parallelepiped.

Rock and similar type samples, e.g., concrete, have relatively high acoustic

attenuation, or low  $Q$ . Thus several very practical issues arise. (d) How do we cause resonance peaks to separate enough to be distinguishable? (e) How do we acquire the most information out of the first measurable resonance peaks, i.e., how do we maximize the dependence of those modes on the elastic constants of interest? (f) To what extent can anisotropy be recognized and determined for an inhomogeneous sample? I will show here, that by altering the sample geometry, while maintaining a rectangular parallelepiped shape, these practical issues can be addressed.

### 3.1 Free boundaries

The variational technique used in the analysis [9] is based on the recognition that the displacement vectors satisfying the elastic wave equation with free boundaries on the sample surface, also make the elastic Lagrangian of the sample stationary. To approximate free boundaries in the experiment, the source and detector are most often placed at vertices of the parallelepiped, delicately supporting the sample. The sample is nearly free standing. Holding the sample at vertices has the further advantage of keeping the transducers away from the expected node lines of the resonant modes. When the full resonance spectrum is complicated, transducers may be placed purposely at expected nodes, such as the center of a face, to temporarily simplify the spectrum. Using transducers for support limits the sample size. Our transducers are PZT-5 piezoelectric pinducers. We have limited our samples to less than  $50\text{ cm}^3$ , and 150 g.

### 3.2 Inhomogeneity

The elastic and acoustic response of a consolidated material is primarily determined by a macroscopic average over the bonds between constituents, rather than by the elastic properties of the constituents themselves. For example, the elastic properties of sandstone, a quartz conglomerate, are more a function of grain-to-grain bond properties than of  $\text{SiO}_2$  properties. We are interested in the elastic properties of consolidated materials, i.e., materials that are inherently inhomogeneous. We want to be able to regard these materials as homogeneous. We adopt the rule of thumb that an inhomogeneous material looks homogeneous to a propagating wave when the wavelength of the wave is much greater than the length scale of the inhomogeneity.

A simple calculation for a one-dimensional system with free boundaries results in resonance wavelengths  $\lambda = 2l/n$ , where  $l$  is the length of the sample and  $n$  is an integer number of nodes. Assuming that we need the first ten resonance frequencies to accurately determine two elastic constants with RUS [5], we want the maximum size of an inhomogeneity  $\xi \ll l_{\min}/5$ , where  $l_{\min}$  is the length of the smallest side of the sample. This estimate is very conservative, since it is highly unlikely that all of the first ten resonant modes in a three-dimensional sample will have nodes along a single direction. We use the ratio  $\xi/l \propto (\text{visible grain size})/(\text{length})$ , to characterize the inhomogeneity of our samples.

### 3.3 Sample geometry, the figure of the sample

Samples of consolidated materials are difficult to machine without chipping, and often do not have perfectly parallel sides. How ideal must the figure of a sample be? This question can be examined using the perturbation treatment of the elasticity problem sketched in Appendix A. To simulate the effect of an error in the figure of a sample, a localized mass is carried around the perimeter of the sample, and the frequency shift caused by this mass is calculated. The frequency shift for mode  $n$  is given by

$$\frac{\omega - \omega_n^2}{\omega_n^2} \approx 2 \frac{\delta f_n}{f_n} = \langle u_n | \delta \rho | u_n \rangle, \quad (3.1)$$

where  $u_n$  and  $\omega_n$  are the eigenmodes and eigenfrequencies of a perfectly shaped sample, and  $\delta \rho$  is the localized mass perturbation being carried around the sample. In Fig. 3.2, the average frequency shift of the first 20 resonances,

$$\delta F = \frac{1}{N} \sqrt{\sum_{n=1}^N \left( \frac{\delta f_n}{f_n} \right)^2}, \quad (3.2)$$

where  $N=20$ , is shown as a function of the perturbation placement. The perturbation is carried along the sample edge and into the sample interior as shown in the inset in the figure. When the perturbation is at an interior point it is essentially a 1% mass distortion, when it is along the perimeter it is a 1% distortion of the figure. Distortions in the figure of the sample are much more important than equivalent mass distortions in the sample interior. A 1% chip out of the corner of a sample can produce a 1% change in the frequency. A 1% mass distortion at the sample center produces less than 0.2% change in frequency.

Given the number of other contributors to error in RUS measurements on

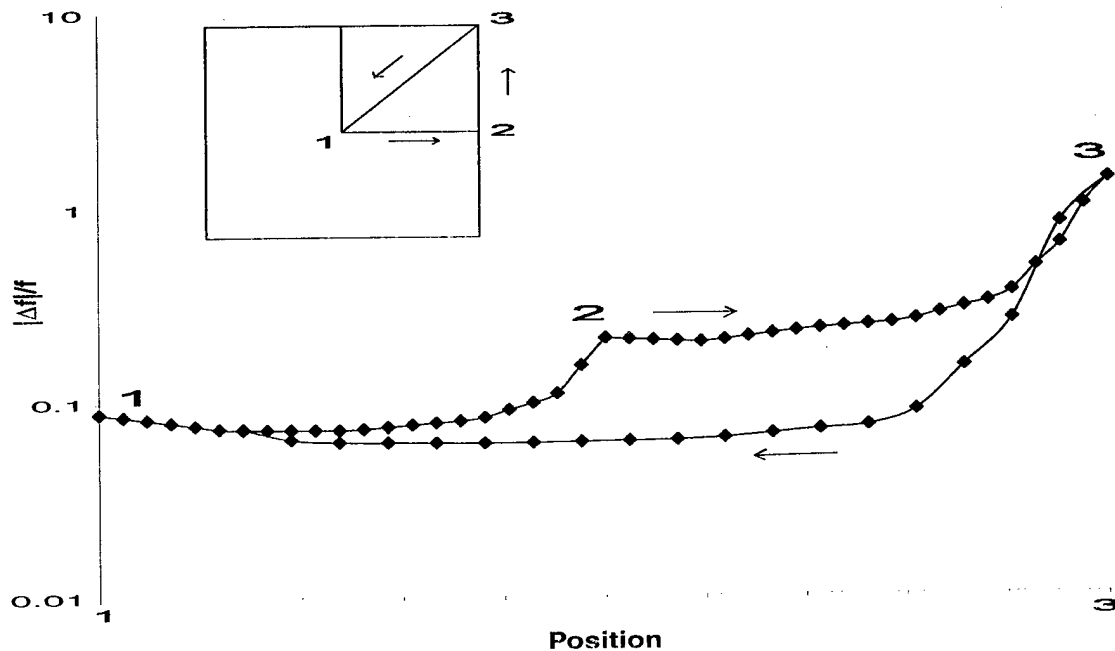


Figure 3.2: Frequency shift as a function of the perturbation placement.

consolidated materials, these contributions to error are rather small. This conclusion was confirmed empirically by making RUS measurements on samples before and after chipping, and on various samples of the same size.

### 3.4 Distinct resonance peaks

Consolidated materials are often characterized by a low quality factor  $Q$ , i.e., a high attenuation. At fixed amplitude low  $Q$  materials have fewer observable resonance frequencies than high  $Q$  materials. Additionally the broader resonance peaks of low  $Q$  materials overlap nearby peaks and complicate peak picking. However, the geometry of a sample sets the frequency difference between peaks. For example, a sample that is a cube of an isotropic material has a three-fold degeneracy in all of its resonance



frequencies. Thus, we can use geometry to minimize peak overlap due to a low  $Q$ .

In Fig. 3.3, calculated resonance frequencies are plotted for a parallelepiped sample as a function of the aspect ratio,  $c/a$ . The volume of the sample is fixed,  $a \times b \times c = 4.8 \text{ cm}^3$ , and  $b = 1.1a$ . Aspect ratios greater than one correspond to rod-like samples and are characterized by the number  $c/a$  in Fig. 3.3. Aspect ratios less than one correspond to plate-like samples and are characterized by the number  $-a/c$  in Fig. 3.3. A homogeneous, isotropic sample with elastic constants appropriate to basalt was assumed. As the aspect ratio is increased, the low lying modes separate. For example, at  $b = 1.1a$ ,  $c/a = 4$ , we expect to be able to pick out fourteen distinct resonances before mode overlap becomes a serious problem for a RUS experiment.

Increasing the aspect ratio further might allow us to pick out even more distinct peaks. However, the RUS inversion code uses a fixed order polynomial to variationally fit modes [9]. As one side of a sample becomes disproportionately large, a disproportionate number of nodes in the normal modes will be in that direction, and the inversion code will lose fitting accuracy in that direction. We have chosen to keep samples at  $1/4 \leq c/a \leq 4$  (-4 to 4 in Fig. 3.3).

### 3.5 $c_{11}$ dependence

A rule of thumb [5] establishing the number of resonances necessary to find elastic constants, is that five resonance frequencies are needed to accurately determine each independent elastic constant. Thus, for an isotropic material described by two elastic constants, we need to experimentally determine the first ten resonance frequencies.

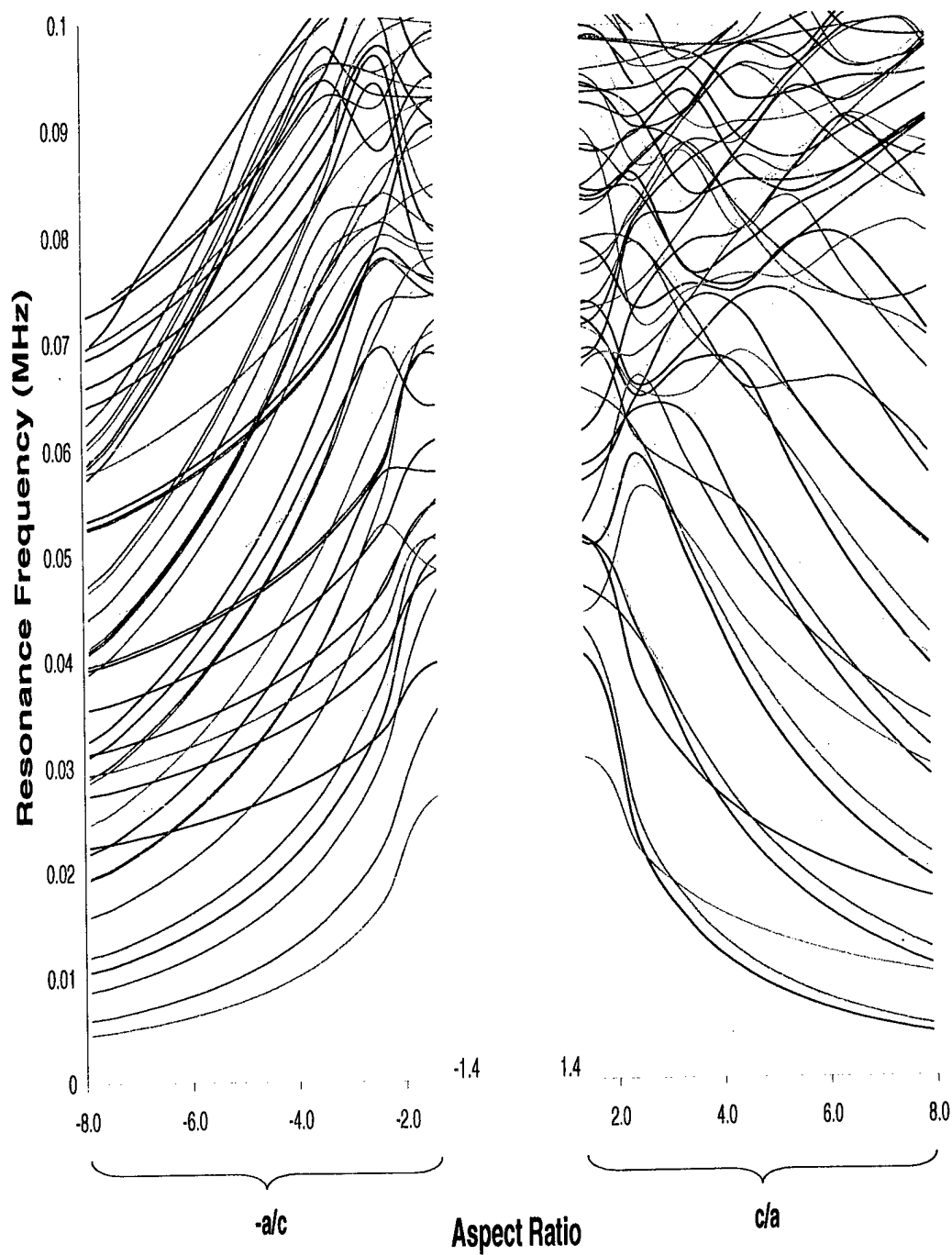


Figure 3.3: Calculated resonance frequencies as a function of aspect ratio. The sample is at a constant volume of 4.8 cc;  $b = 1.1a$ , and the aspect ratio is  $c/a$  on the right side,  $-a/c$  on the left side. The elastic constants are  $c_{11} = 86.6$  GPa and  $c_{44} = 31.9$  GPa.

Certainly the confidence with which the elastic constants can be determined is influenced by the involvement of each elastic constant in the first ten modes of the sample. It is important to mention that the first ten resonance peaks lie within a 100 kHz range. Due to this relatively small frequency range, the effects of dispersion have been ignored.

Since  $c_{11} \approx 2c_{44}$ , we expect low frequency modes to be more highly dependent on  $c_{44}$  than  $c_{11}$  (in analogy to the frequencies of the modes of a soft spring versus a stiff spring network). Indeed, for a cubic shaped sample of basalt, the first eight resonance frequencies have a total dependence on  $c_{11}$  of less than 15%. That is, most low lying modes are shear modes, involving very little compression. However, the geometry of the sample influences  $c_{11}$  dependence in the resonance modes. Plate-like and rod-like samples will have low-lying bending or flexural modes that are compressional in nature.

In Fig. 3.4, the  $c_{11}$  dependence of the first ten resonant modes of a parallelepiped sample are shown as a function of the ratio of the longest side to the shortest side of the sample  $c/a$ . Positive aspect ratios denote rod-like samples (the aspect ratio is  $c/a$  on the right side); negative aspect ratios denote plate-like samples (the aspect ratio is  $-a/c$  on the left side). These dependencies are found by taking the derivative of the frequency with respect to each of the moduli. A homogeneous, isotropic sample with elastic constants appropriate to basalt was assumed. As the aspect ratio is increased, the  $c_{11}$  dependence increases. For example, for a sample with  $c/a = 4$ , seven of the first ten modes have a  $c_{11}$  dependence over 20%, as opposed to only two

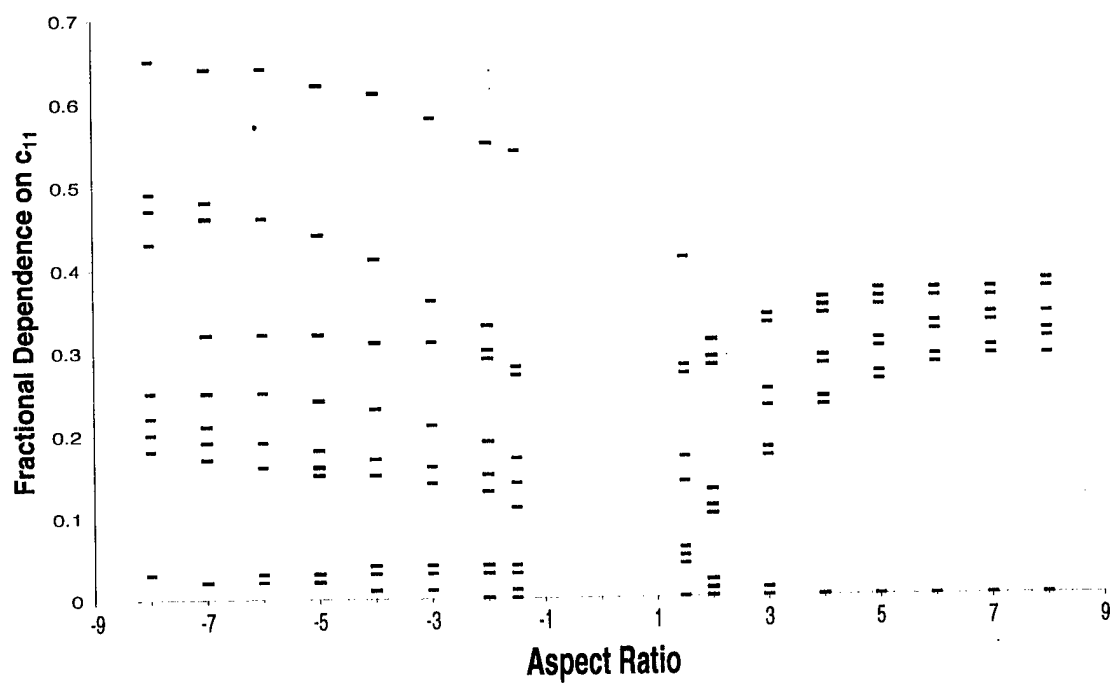


Figure 3.4:  $c_{11}$  dependence as a function of aspect ratio. The sample is at a constant volume of 4.8 cc;  $b = 1.1a$ , and the aspect ratio is  $c/a$  on the right side,  $-a/c$  on the left side. The elastic constants are  $c_{11} = 86.6$  GPa and  $c_{44} = 31.9$  GPa.

modes for  $c/a = 1$ .

### 3.6 Anisotropy

If isotropic symmetry is broken in a single direction, the sample has hexagonal symmetry and is called transversely isotropic. Many consolidated materials, such as sedimentary rock and laminar systems, are transversely isotropic. Hexagonal symmetry is described by five independent elastic constants (i.e.,  $c_{11}$ ,  $c_{33}$ ,  $c_{13}$ ,  $c_{44}$ ,  $c_{66}$ ). Thus, in order to determine hexagonal symmetry using RUS, we might expect to need 25 resonance frequencies. This is a prohibitively large number for low  $Q$  samples. Do we actually need this many? Suppose we have 10 measured resonances. Can we detect anisotropy with these modes? The following is a test of the sensitivity of RUS to anisotropy.

Consider the elastic system described by the elastic tensor

$$M = \begin{pmatrix} c_{11} & c_{12} & c_{13} & 0 & 0 & 0 \\ c_{12} & c_{11} & c_{13} & 0 & 0 & 0 \\ c_{13} & c_{13} & c_{33} & 0 & 0 & 0 \\ 0 & 0 & 0 & c_{44} & 0 & 0 \\ 0 & 0 & 0 & 0 & c_{44} & 0 \\ 0 & 0 & 0 & 0 & 0 & c_{66} \end{pmatrix}, \quad (3.3)$$

where

$$\begin{aligned}
 c_{11} &= (1 + \varepsilon) C_0, \\
 c_{12} &= 0.4 (1 - 2\varepsilon) C_0, \\
 c_{13} &= 0.4 (1 + \varepsilon) C_0, \\
 c_{33} &= (1 - 2\varepsilon) C_0, \\
 c_{44} &= 0.3 (1 - 1.5\varepsilon) C_0, \\
 c_{66} &= 0.3 (1 + 3\varepsilon) C_0,
 \end{aligned} \tag{3.4}$$

$0 \leq \varepsilon \leq 0.25$ ,  $C_0 = 10^{11}$  dynes/cm<sup>2</sup>, and  $\rho_0 = 1$  gm/cm<sup>3</sup>. As  $\varepsilon$  varies from 0 to 0.25 the elastic tensor varies from isotropic

$$M(0) = C_0 \begin{pmatrix} 1 & 0.4 & 0.4 & 0 & 0 & 0 \\ 0.4 & 1 & 0.4 & 0 & 0 & 0 \\ 0.4 & 0.4 & 1 & 0 & 0 & 0 \\ 0 & 0 & 0 & 0.3 & 0 & 0 \\ 0 & 0 & 0 & 0 & 0.3 & 0 \\ 0 & 0 & 0 & 0 & 0 & 0.3 \end{pmatrix}, \tag{3.5}$$

to hexagonal

$$M(0.25) = C_0 \begin{pmatrix} 1.25 & 0.2 & 0.5 & 0 & 0 & 0 \\ 0.2 & 1.25 & 0.5 & 0 & 0 & 0 \\ 0.5 & 0.5 & 0.5 & 0 & 0 & 0 \\ 0 & 0 & 0 & 0.1875 & 0 & 0 \\ 0 & 0 & 0 & 0 & 0.1875 & 0 \\ 0 & 0 & 0 & 0 & 0 & 0.525 \end{pmatrix}. \tag{3.6}$$

These numbers have been chosen so that the average properties of the tensor are the same while the system is shifting from isotropic to hexagonal with the change in  $\varepsilon$ .

By average, we mean that the first three diagonal components ( $c_{11}, c_{22}, c_{33}$ ) average to  $C_0$ ; the three off-diagonal elements ( $c_{12}, c_{13}, c_{23}$ ) average to  $0.4C_0$ ; and the last three diagonal elements ( $c_{44}, c_{55}, c_{66}$ ) average to  $0.3C_0$ , regardless of the value of  $\varepsilon$ . For  $\varepsilon = 0.25$  the elastic matrix is approximately that of zinc [14].

We proceed as follows:

1. Choose values of  $c/a$ , and  $\varepsilon$ .
2. Calculate the lowest 10 frequencies,  $g_1, \dots, g_{10}$ , using the elastic tensor in Eqs. (3.3) and (3.4).  $g_1, \dots, g_{10}$  are the frequencies of the **model system**.
3. Assume the model system is isotropic and the frequencies  $g_1, \dots, g_{10}$  are the measured frequencies of the lowest 10 modes, the data.
4. Fit the model system data with an isotropic model, i.e., with  $c_{11}$  and  $c_{44}$ .

In Fig. 3.5 the frequency error is shown

$$F = \frac{1}{N} \sqrt{\sum_{n=1}^N (f_n - g_n)^2}, \quad (3.7)$$

as a function of  $\varepsilon$ , where  $N = 10$ , for  $-4(1/4) < c/a < 4$ , and  $c/a$  is the ratio of the longest ( $c$ ) to shortest ( $a$ ) sides. Aspect ratios less than one are represented as negative reciprocals, e.g.,  $c/a = 1/4$  is represented as  $c/a = -4$ . For a  $c/a$  ratio of 4 we see that the error due to attempting an isotropic fit to data from an anisotropic sample remains less than 1% for  $\varepsilon < 0.22$ . If we choose 1% error as the threshold between a good fit and a bad fit, we do not have enough information about the elastic properties of the system to recognize that it is not isotropic if we are given only the

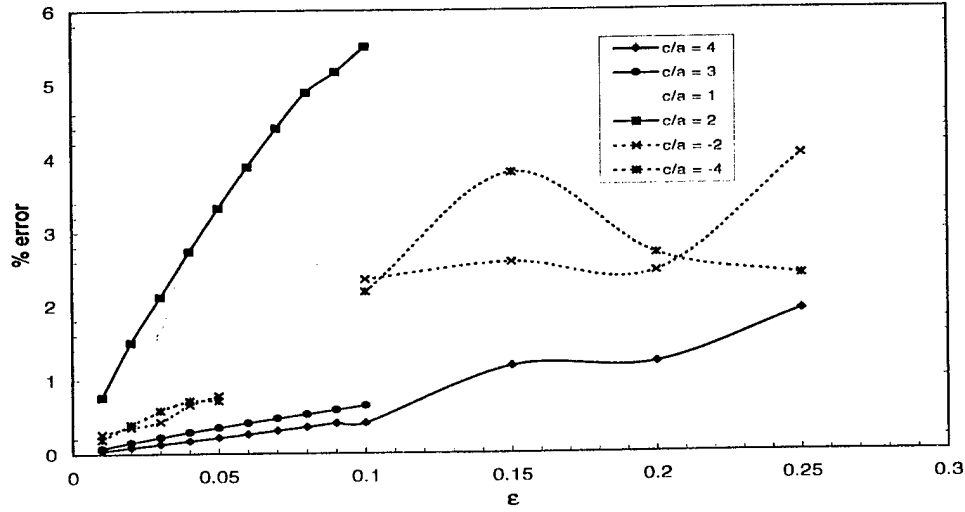


Figure 3.5: Frequency error vs.  $\varepsilon$  for  $c/a = -4, -2, 1, 2, 3, 4$ .

first 10 modes. In practice the choice of a suitable threshold must be empirically determined.

The  $c/a = 2$  results in Fig. 3.5 seems to imply that this aspect ratio provides the best detection of anisotropy. Figures 3.6 and 3.7 show a measure of the sharpness of the minimum in  $F$ , through the use of error ellipses, for two of the solutions in Fig. 3.5 ( $c/a=4$ ,  $c/a=2$ ). In these figures the  $(c_{11}/c_{11}^{(0)}, c_{44}/c_{44}^{(0)})$  pair for which the frequency error is a minimum, is plotted (black dot) for  $0 \leq \varepsilon \leq 0.1$  where  $c_{11}^{(0)} = C_0$  and  $c_{44}^{(0)} = 0.3C_0$ . Anisotropy is increasing from the top right to the lower left. The black dots are the result of an isotropic fit. The red ellipses represent a measure of the uncertainty in the isotropic fits (the sharpness of the corresponding minima). It follows that for  $c/a = 4$ , the isotropic fit is very accurately determined when  $c_{11}/c_{11}^{(0)}$  approaches 1, while the uncertainty grows as we decrease that ratio (increase  $\varepsilon$ ). From



Figure 3.6: A measure of the quality of fit (sharpness of the minimum) for  $c/a=4$  and an increasing variation from isotropy.

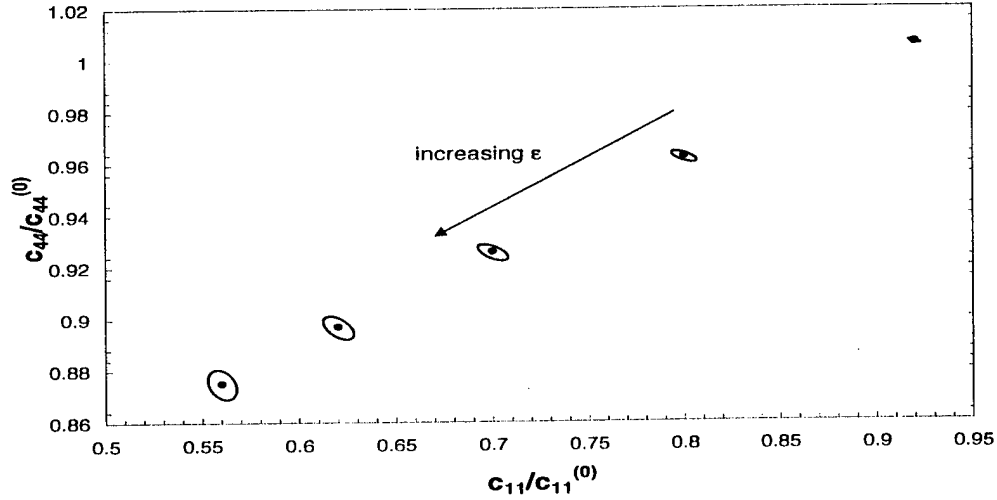


Fig. 3.6 we see that for aspect ratio 4 the minimum in the frequency error is sharply defined. Contrast this to Fig. 3.7 for aspect ratio 2. For this case the frequency error is not at all sharply defined. With aspect ratio 2 the frequency error is neither small (note it is less than 1% for  $\varepsilon < 0.06$ ) nor sharply determined.

At  $\varepsilon = 0.09$  (Fig. 3.8) there are 6 points and their associated error ellipses labeled 5, 10, 15, 20, 25, and 30. These points represent the frequency error for  $c/a = 4$  found for isotropic fits of  $N = 5, \dots, 30$  anisotropic frequencies. Here we are investigating the ability to see anisotropy from an isotropic model, as the number of frequencies increases. The differences in the sharpness of the minima (size of the error ellipses) give a very good indication of how the ability to discriminate increases with an increasing number of frequencies. We argue that for  $N > 15$  one begins to

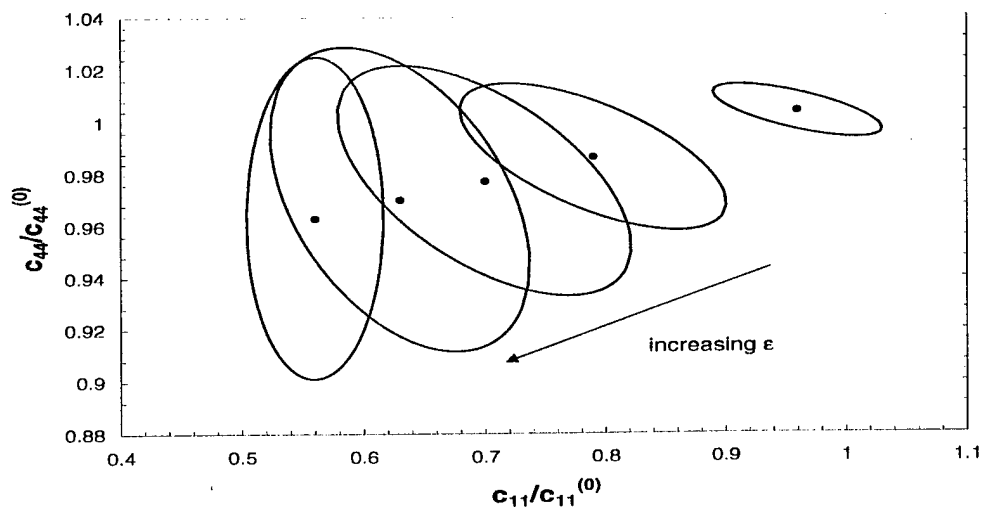


Figure 3.7: A measure of the quality of fit (sharpness of the minimum) for  $c/a=2$  and an increasing variation ( $\epsilon$ ) from isotropy.

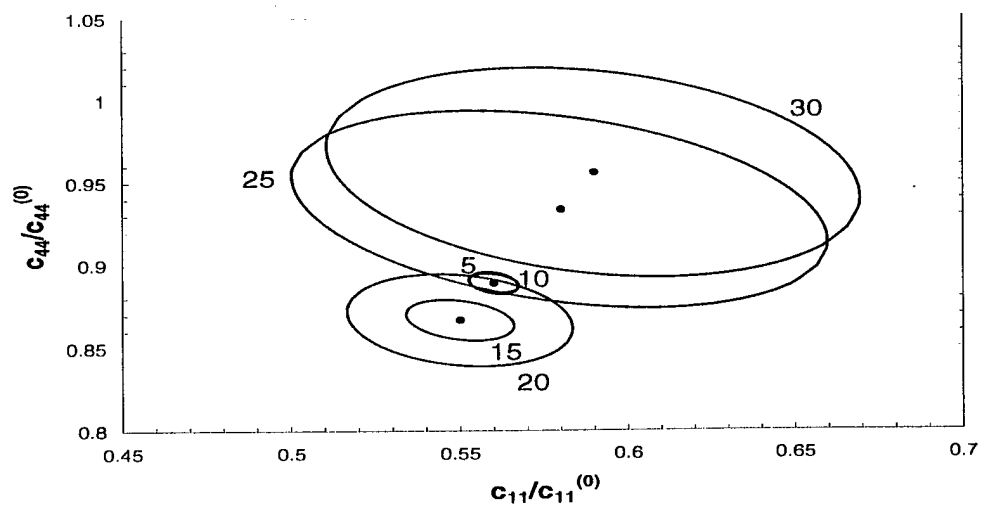


Figure 3.8: A measure of the quality of fit (sharpness of the minimum) for  $c/a=4$ ,  $\epsilon=0.09$  and a varying number of measured resonance frequencies ( $f = 5, 10, 15, 20, 25, 30$  as labeled).

see errors great enough to indicate that the sample is not isotropic.

Thus RUS is capable of distinguishing a deviation from isotropy, given a sufficient number of resonance frequencies. A sample with  $c/a = 2$ , displays large errors at small anisotropic deviations, as well as very shallow minima in the frequency fits, thus giving us an idea of the goodness of fit, or rather that they don't fit. For higher Q materials, the best method of detecting anisotropy may be to simply measure more peaks, however, when the number of resonance frequencies is limited to 10, the sample size should have  $c/a = 2$  (assuming  $b = 1.1a$ ) to have the greatest sensitivity to the anisotropy.

## Chapter 4

# EXPERIMENTAL RESULTS AND CONCLUSIONS

The previous chapters have provided a foundation with which we can now investigate real samples. Using the analytical method described in Chap. 2, and the techniques for optimizing our results discussed in Chap. 3, we have performed RUS experiments on a variety of rock types, and sizes. A case study of a sample of black gabbro is detailed in Appendix B, documenting the process of applying RUS to inhomogeneous samples.

### 4.1 Results

RUS experiments and analysis were performed on samples of berkeley blue granite, pink quartzite, and black gabbro in sample set 1 (Table 4.1). Figure 4.1 provides a pictorial representaion of sample set 1. Sample set 2 consists of an assort-

Table 4.1: Sample Set 1

Rock Type	ID	$a$ (cm)	$b/a$	$c/a$	$\xi/a$	$Q$	$c_{11}$ (GPa)	$c_{44}$ (GPa)	%error
Black Gabbro	BG-1	2.8	1.1	1.4	0.23	350	96	36	0.557
Black Gabbro	BG-2	2.3	1.1	2.6	0.28	350	97	36	0.703
Black Gabbro	BG-3	1.0	1.1	4.0	0.32	350	107	35	0.377
Black Gabbro	BG-4	1.3	1.1	4.0	0.24	350	106	35	0.377
Black Gabbro	BG-5	1.6	1.1	4.0	0.31	350	119	35	0.489
Black Gabbro	BG-6	2.0	1.1	4.0	0.21	350	107	36	0.279
Pink Quartzite	PQ-1	2.0	1.1	4.0	1.68	250	69.6	35.1	1.271
Berkeley Blue Granite	BB-1	2.0	1.1	4.0	0.20	230	30.7	12.3	13.28

ment of basalt, sierra white granite, and black gabbro. Isotropy was assumed for all samples. The results are tabulated in order of increasing aspect ratio  $c/a$ . To crudely determine the size of inhomogeneity  $\xi$  in each sample, the largest surface structure (blob) on each sample was measured. In sample set 1 cases, the first ten resonance frequencies were used for the fit. The average  $Q$  is determined from  $Q = \omega/\Delta\omega$  averaged over the first ten resonances, where  $\omega$  is the resonance frequency, and  $\Delta\omega$  is the full-width at half-maximum of the resonance intensity. Note that the RMS percent error is strongly dependent on  $c/a$ ,  $a/\xi$ , and  $Q$ . High values of these parameters lead to better fits between measured and calculated resonances.

Notice that for all black gabbro samples in sample set 1, the shear modulus ( $c_{44}$ ) is consistently 35-36 GPa. This agreement between samples indicates that the measured resonances have an adequate dependence on  $c_{44}$ . However, there is a marked difference between the compressive modulus ( $c_{11}$ ) for samples having an aspect ratio  $c/a = 4$  and those for which  $c/a < 4$ . The error for the samples with  $c/a < 4$  is also greater than for the  $c/a = 4$  samples. This indicates that the lack of  $c_{11}$  dependence

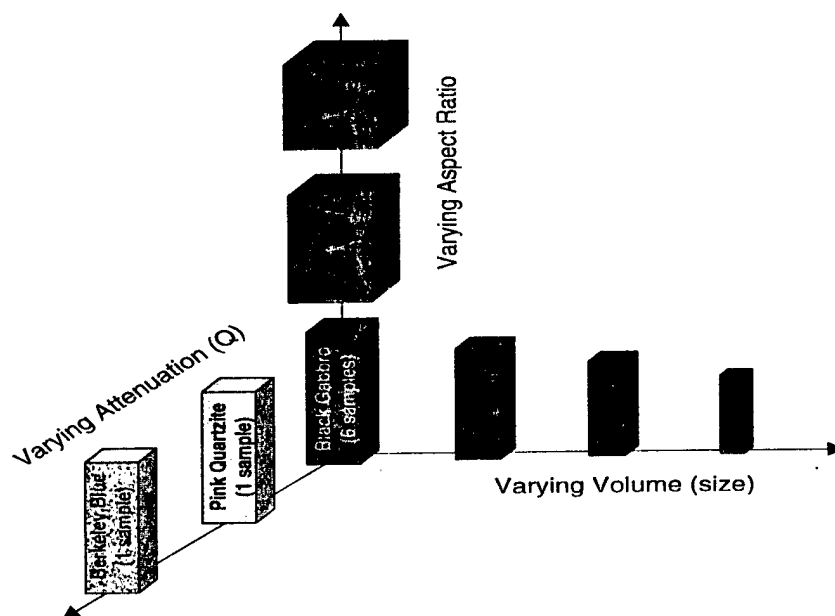


Figure 4.1: Pictorial representation of sample set 1.

Table 4.2: Sample Set 2

Rock Type	ID	$a$ (cm)	$b/a$	$c/a$	$\xi/a$	$Q$	$c_{11}$ (GPa)	$c_{44}$ (GPa)	%error
Sierra White Granite	SW-1	3.7	1.1	1.5	0.18	145	37.6	18.7	1.238
Sierra White Granite	SW-2	2.8	1.1	1.6	0.24	140	43.2	18.6	2.023
Sierra White Granite	SW-3	1.0	1.25	3.3	0.46	150	20.8	21.3	17.29
Sierra White Granite	SW-4	1.7	1.2	4.0	0.17	140	37.5	19.1	0.630
Basalt	B-1	2.1	1.1	1.5	0.29	275	88.1	31.3	0.632
Basalt	B-2	2.7	1.0	1.7	0.14	240	88.4	31.7	0.632
Basalt	B-3	2.8	1.1	2.0	0.04	255	87.3	31.6	0.709
Basalt	B-4	1.7	1.1	4.0	0.06	335	87.2	31.5	0.313

in the low-lying modes for the more compact samples is effecting the final result, as we expected from our modeling in Sec. 3.5. Sample SW-2 (Table 4.2) also demonstrates this phenomena as is shown from the larger fit error and the slightly higher value for  $c_{11}$  compared to the  $c_{11}$  value of samples SW-1 and SW-4.

Sample set 1 also illustrates the effects of decreasing  $Q$ . The fits for samples BB-1 and PQ-1 (low  $Q$ ) have a substantially larger % error than the BG sample fits (high  $Q$ ). It is interesting to note, however, that while the sample BB-1 fit has a 13% error, the commonly accepted values for  $c_{11}$  and  $c_{44}$  are 30 GPa and 13 GPa, respectively. Thus even though the fitting error is high, the moduli determined from the fit are quite accurate. It is important to remember that results from the RUS inversion are the best possible answers for the given data. The % error is an uncertainty level, not an a measure of the difference between real and determined values of the moduli.

In sample set 2, we have a random distribution of aspect ratios. Here we can see similar results as for sample set 1. As for the black gabbro samples above, both Sierra white granite and basalt give results with lower percent error for samples having an aspect ratio  $c/a = 4$ . Also we again see close agreement in the shear modulus between samples of the same material.

Sample SW-3 is an interesting sample in that it is the only SW sample that exhibits a high percent error, and whose moduli deviate from the other SW samples. This is not surprising as we look at the size of the inhomogeneity in the sample. In Sec. 3.2 we stated that the relative size of the inhomogeneities ( $\xi/a$ ) cannot exceed

1/5 (0.2). Sample SW-3 has a  $\xi/a$  value of 0.46, more than twice that of what should be allowed. In this sample inhomogeneity prevents us from determining the average elastic moduli. The value for  $\xi/a$  given in Sec. 3.2 is actually a conservative value, as the model used was one-dimensional. In a three dimensional elastic solid, the first ten resonances will not all be along the same dimension, and thus a larger inhomogeneity could be tolerated. This would explain why the BG samples all exhibit a low % error yet have  $\xi/a$  values slightly above 0.2.

## 4.2 Conclusions

The modeling in Chap. 3 and the results shown in Tables 4.1 and 4.2 indicate that RUS is a viable technique for characterizing the average elastic behavior of inhomogeneous materials. Although larger RMS errors can be expected for inhomogeneous materials than those acceptable in the single crystal business ( $< 0.5\%$  [5]), our results are generally close for different samples of the same material, and consistent with accepted values [15].

For RUS on rock samples to be a viable technique, it must be developed further, specifically to the needs of the field of geophysics. For example, we need to develop RUS for cylindrical sample geometry, so that it is capable of accepting a standard core sample. The symmetry of cylinders poses new problems that will be considered in the future. Also we plan to take a more in-depth look at the possibility of detecting and analyzing anisotropic systems. Finally we plan to develop an environmental control chamber inside which the RUS experiment can be conducted. The chamber will allow



us to introduce two new variables to the experiment, temperature and water vapor pressure. The chamber design is currently that of a sealed vacuum oven in which we can easily achieve 250°C (423 K), and enclose standard saturation salts.

With these new additions to the work that has been completed here, we expect to develop a new use for RUS in geophysics. We will be able to explore the elastic responses of materials in the earth's crust under various temperature and saturation conditions.

# Appendix A

## PERTURBATION THEORY

The elastic energy of a solid body, in steady state at frequency  $\omega$ , is described by the Lagrangian

$$L = \int d\mathbf{x} \phi(\mathbf{x}) \left( \frac{\omega^2}{2} \rho(\mathbf{x}) u_i^2 - \frac{1}{2} c_{ijkl}(\mathbf{x}) \frac{\partial u_i}{\partial x_j} \frac{\partial u_k}{\partial x_l} \right), \quad (\text{A.1})$$

where  $\mathbf{u}$  is the displacement vector at position  $\mathbf{x}$ ,  $c_{ijkl}$  is the elastic tensor,  $\rho$  the mass density, repeated indices are summed over the cartesian coordinates, and  $\phi$  describes the extent or figure of the sample,

$$\phi(\mathbf{x}) = \begin{cases} 1 & \mathbf{x} \text{ inside the sample} \\ 0 & \mathbf{x} \text{ outside the sample} \end{cases} \quad (\text{A.2})$$

Equation (A.1) is quite general, allowing for (1) an arbitrary sample figure  $\phi(\mathbf{x})$  (2) a nonuniform density  $\rho(\mathbf{x})$ , and (3) a non uniform elastic tensor  $c_{ijkl}(\mathbf{x})$ .

The equation of motion for the normal modes is found by varying  $L$  with respect to  $u_i$ . If the traction on the surfaces defined by  $\phi(\mathbf{x})$  vanishes,  $u_i$  satisfies a

wave equation in the form

$$\rho(\mathbf{x})\omega^2 u_i + \frac{\partial}{\partial x_j} \left( c_{ijkl}(\mathbf{x}) \frac{\partial u_k}{\partial x_l} \right) = 0 \quad (\text{A.3})$$

for  $\mathbf{x}$  inside of the sample. The condition that the traction on the surfaces vanish is enforced by holding the sample so that it is effectively free standing.

The equation of motion for  $u_i$ , Eq. (A.3), can be cast in the form of a variational problem [16]. That is, the quantity  $\omega^2[u_i]$ , where

$$\omega^2[u_i] = \frac{\int d\mathbf{x} \phi(\mathbf{x}) c_{ijkl}(\mathbf{x}) \frac{\partial u_i}{\partial x_j} \frac{\partial u_k}{\partial x_l}}{\int d\mathbf{x} \phi(\mathbf{x}) \rho(\mathbf{x}) u_i^2}, \quad (\text{A.4})$$

must be stationary subject to arbitrary variations of  $u_i$  consistent with traction free boundaries. Using this form for the normal mode frequencies it is possible to make a systematic study of the consequences of change in  $\phi(\mathbf{x})$ ,  $\rho(\mathbf{x})$ , and  $c_{ijkl}(\mathbf{x})$ . Assume the ideal sample is a rectangular parallelepiped specified by  $\phi_0$ , has uniform density  $\rho_0$ , and has uniform elastic constants  $c_{ijkl}^0$ . Then variations in these quantities are given by  $\delta\phi(\mathbf{x}) = \phi(\mathbf{x}) - \phi_0$ ,  $\delta\rho(\mathbf{x}) = \rho(\mathbf{x}) - \rho_0$  and  $\delta c_{ijkl}(\mathbf{x}) = c_{ijkl}(\mathbf{x}) - c_{ijkl}^0$ . To first order in  $\delta\phi$ ,  $\delta\rho$ , and  $\delta c$  we have

$$\omega^2 = \frac{N_0}{D_0} \left[ 1 + \frac{\delta N_c}{N_0} + \frac{\delta N_\phi}{N_0} - \frac{\delta D_\rho}{D_0} - \frac{\delta D_\phi}{D_0} \right] \quad (\text{A.5})$$

where

$$N_0 = c_{ijkl}^0 \int d\mathbf{x} \phi_0 \frac{\partial u_i}{\partial x_j} \frac{\partial u_k}{\partial x_l}, \quad (\text{A.6})$$

$$D_0 = \rho_0 \int d\mathbf{x} \phi_0 u_i^2, \quad (\text{A.7})$$

$$\delta N_c = \int d\mathbf{x} \phi_0 (c_{ijkl}(\mathbf{x}) - c_{ijkl}^0) \frac{\partial u_i}{\partial x_j} \frac{\partial u_k}{\partial x_l}, \quad (\text{A.8})$$

$$\delta N_\phi = c_{ijkl}^0 \int d\mathbf{x} (\phi(\mathbf{x}) - \phi_0) \frac{\partial u_i}{\partial x_j} \frac{\partial u_k}{\partial x_l}, \quad (\text{A.9})$$

$$\delta D_\rho = \int d\mathbf{x} \phi_0 (\rho(\mathbf{x}) - \rho_0) u_i^2, \quad (\text{A.10})$$

$$\delta D_\phi = \rho_0 \int d\mathbf{x} (\phi(\mathbf{x}) - \phi_0) u_i^2. \quad (\text{A.11})$$

Using the variational technique of Visscher et al. we can find the eigenvalues  $\omega_{\nu,0}^2 = N_0/D_0$  and eigenfunctions  $u_{i,\nu}^0 = \psi_\nu(\mathbf{x})$  associated with the ideal sample. Thus the lowest order contribution to the frequency shift due to a perturbation is

$$\frac{\omega_\nu^2 - \omega_{\nu,0}^2}{\omega_{\nu,0}^2} = \frac{\delta N_c}{N_0} + \frac{\delta N_\phi}{N_0} - \frac{\delta D_\rho}{D_0} - \frac{\delta D_\phi}{D_0} \quad (\text{A.12})$$

where  $u_i = \psi_\nu(\mathbf{x})$ . For the example of an inhomogeneous mass density we would have

$$\frac{\omega_\nu^2 - \omega_{\nu,0}^2}{\omega_{\nu,0}^2} = - \frac{\int d\mathbf{x} \phi_0 (\rho(\mathbf{x}) - \rho_0) |\psi_\nu(\mathbf{x})|^2}{\rho_0 \int d\mathbf{x} \phi_0 |\psi_\nu(\mathbf{x})|^2} \quad (\text{A.13})$$

where

$$\omega_{\nu,0}^2 = \frac{c_{ijkl}^0 \int d\mathbf{x} \phi_0 \frac{\partial \psi_\nu(\mathbf{x})}{\partial x_j} \frac{\partial \psi_\nu(\mathbf{x})}{\partial x_l}}{\rho_0 \int d\mathbf{x} \phi_0 |\psi_\nu(\mathbf{x})|^2}. \quad (\text{A.14})$$

Equation (A.13) is used in Sec. 3.3 for the case of a mass defect to illustrate the consequences of a mass inhomogeneity on resonant mode frequencies.

# Appendix B

## CASE STUDY

In this appendix we will document a complete experiment from the forward calculation to final result. We chose to work with black gabbro for its relatively high homogeneity and  $Q$ . Figures B.1 and B.2 demonstrate why high  $Q$ 's are important. In Fig. B.1, a sample spectrum for stainless steel ( $Q > 1000$ ) is shown; in Fig. B.2 a sample spectrum of Berea sandstone ( $Q \approx 50$ ) is shown. The spectrum in Fig. B.1 shows the resonance frequencies very clearly. The first 15 resonances are very easy to pick. In contrast, the spectrum given in Fig. B.2 contains what appears to be a lot of noise. Consequently the first 15 resonances are difficult to discern. Most rocks have resonance spectra that look more like Berea sandstone than stainless steel. In this study we have limited ourselves to high  $Q$  rocks ( $Q > 150$ ).

The particular sample of Black Gabbro analyzed in this appendix is the fourth black gabbro sample characterized in Chap. 4, Table 4.1. This sample, designated BG-

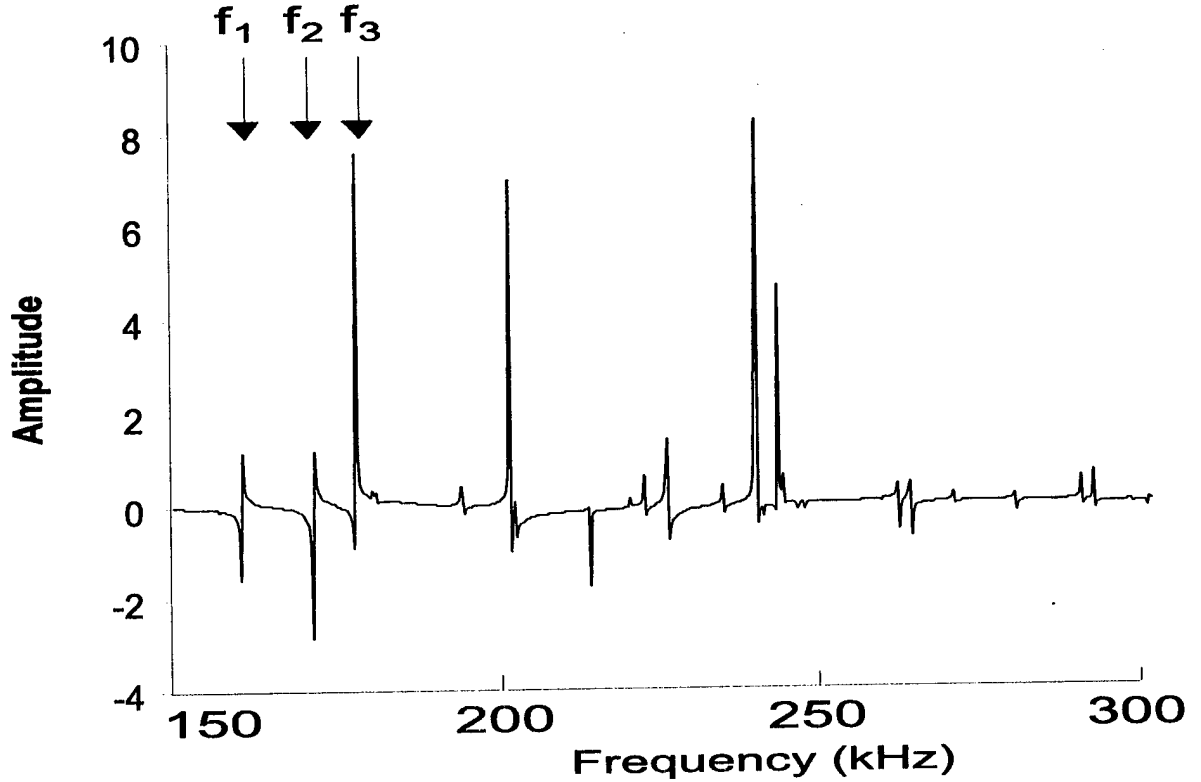


Figure B.1: Example of a spectrum for a stainless steel. Note the sharp peaks (high  $Q$ ).

4, has dimensions  $1.29 \times 1.40 \times 5.01 \text{ cm}^3$ , aspect ratios of  $c/a = 4$  and  $b/a = 1.1$ , mass 26.18 g, and largest observable inhomogeneity  $\xi = 0.47 \text{ cm}$ . The dimensions, mass, and an initial guess for the elastic constants ( $c_{11} = 86.6 \text{ GPa}$ ,  $c_{44} = 31.9 \text{ GPa}$ ) are the input for a numerical forward calculation of resonance frequencies. This input file is shown in Fig. B.3. The output from the forward calculation (also shown in Fig. B.3) displays the first 15 resonance frequencies in MHz, and their fractional dependence upon the two independent moduli ( $df/d(\text{moduli})$  columns,  $c_{11}$ ,  $c_{44}$  respectively). Note that the first ten resonances are well separated and have a strong dependence on the compressional modulus  $c_{11}$ . This is largely due to our choice of aspect ratio  $c/a = 4$ , as suggested by our numerical studies.

This output file provides an initial range of frequencies to guide the experiment.

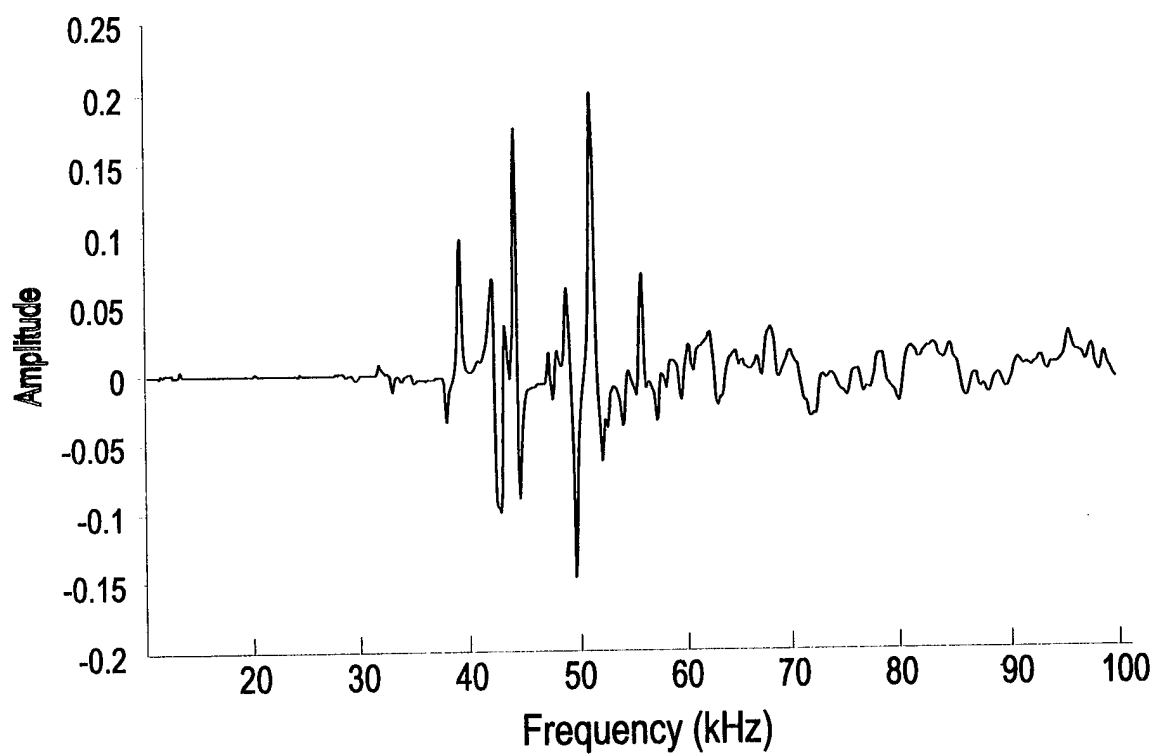


Figure B.2: Example of a spectrum for Berea sandstone. Note the broad overlapping peaks (low  $Q$ ).

Based on the results in Fig. B.3 the first frequency scan (Fig. B.4) was performed over the range 20-100 kHz. This range was expected to contain the first ten resonances and still allow for a shift in those resonances from the predicted values. The first broad sweep of frequencies reveals what appears to be nine of the ten frequencies that the forward calculation led us to expect. To accurately determine the experimental resonance frequencies, we narrowed successive scans to the regions labeled A-G on Fig. B.4.

Accurate determination of the lowest frequency is very important, as the first resonant mode depends heavily on  $c_{11}$  (see Fig. B.3). Since  $c_{11}$  dependence in resonant modes is often difficult to achieve, but is necessary for accurate determination of  $c_{11}$ , it is essential that we find the first resonance of the sample. Missing peaks can be accounted for in the analysis with null entries, but influence the accuracy of our experiment. In Fig. B.5 (region A in Fig. B.4) we see that what appeared to be a single peak is actually two closely spaced peaks. Adjusting the phase of the scan (seen in the upper left window of each scan) brings the peaks out more prominently for selection. The selected resonances occur at 24.6 kHz, 26.0 kHz. These values are shifted from the expected values (22.8 kHz, 24.2 kHz), indicating that one or more of the values entered in the forward calculation are incorrect. Re-measuring and weighing the sample, we found no error in the measurements. Consequently we assume that our initial guess of elastic constants is not accurate.

Scanning regions A-G in turn (Figs. B.5- B.11), pinpointed each of the expected resonance frequencies without confusion due to artifacts or induced noise. In



**Forward Calculation Input File:**

BG-4  
 2 3 10 15 26.18 1.00 1  
 .866 .319  
 5.01 1.29 1.4

**Resulting Output File:**

BG-4  
 free moduli are c11, c44  
 using 10 order polynomials      mass= 26.1800 gm    rho= 2.893 gm/cc

n	fex	fr	%err	wt	k	i	df/d(moduli)
1	1.000000	0.022814	-97.72	1.00	7	2	0.35 0.65
2	1.000000	0.024163	-97.58	1.00	6	2	0.34 0.66
3	1.000000	0.030326	-96.97	1.00	4	1	0.00 1.00
4	1.000000	0.050743	-94.93	1.00	3	2	0.29 0.71
5	1.000000	0.051376	-94.86	1.00	5	1	0.36 0.64
6	1.000000	0.052610	-94.74	1.00	2	2	0.28 0.72
7	1.000000	0.060601	-93.94	1.00	8	2	0.00 1.00
8	1.000000	0.081655	-91.83	1.00	7	3	0.24 0.76
9	1.000000	0.083553	-91.64	1.00	6	3	0.23 0.77
10	1.000000	0.090749	-90.93	1.00	4	2	0.00 1.00
11	1.000000	0.101677	-89.83	1.00	1	2	0.27 0.73
12	1.000000	0.109945	-89.01	1.00	2	3	0.13 0.87
13	1.000000	0.110721	-88.93	1.00	3	3	0.16 0.84
14	1.000000	0.121978	-87.80	1.00	8	3	0.01 0.99
15	1.000000	0.131907	-86.81	1.00	4	3	0.06 0.94

Bulk Modulus=      0.441

c11	c22	c33	c23	c13	c12	c44	c55	c66
0.8660	0.8660	0.8660	0.2280	0.2280	0.2280	0.3190	0.3190	0.3190

d1	d2	d3
5.01000	1.29000	1.40000

Figure B.3: Input file for sample BG-4, forward calculation, and the resulting output file.

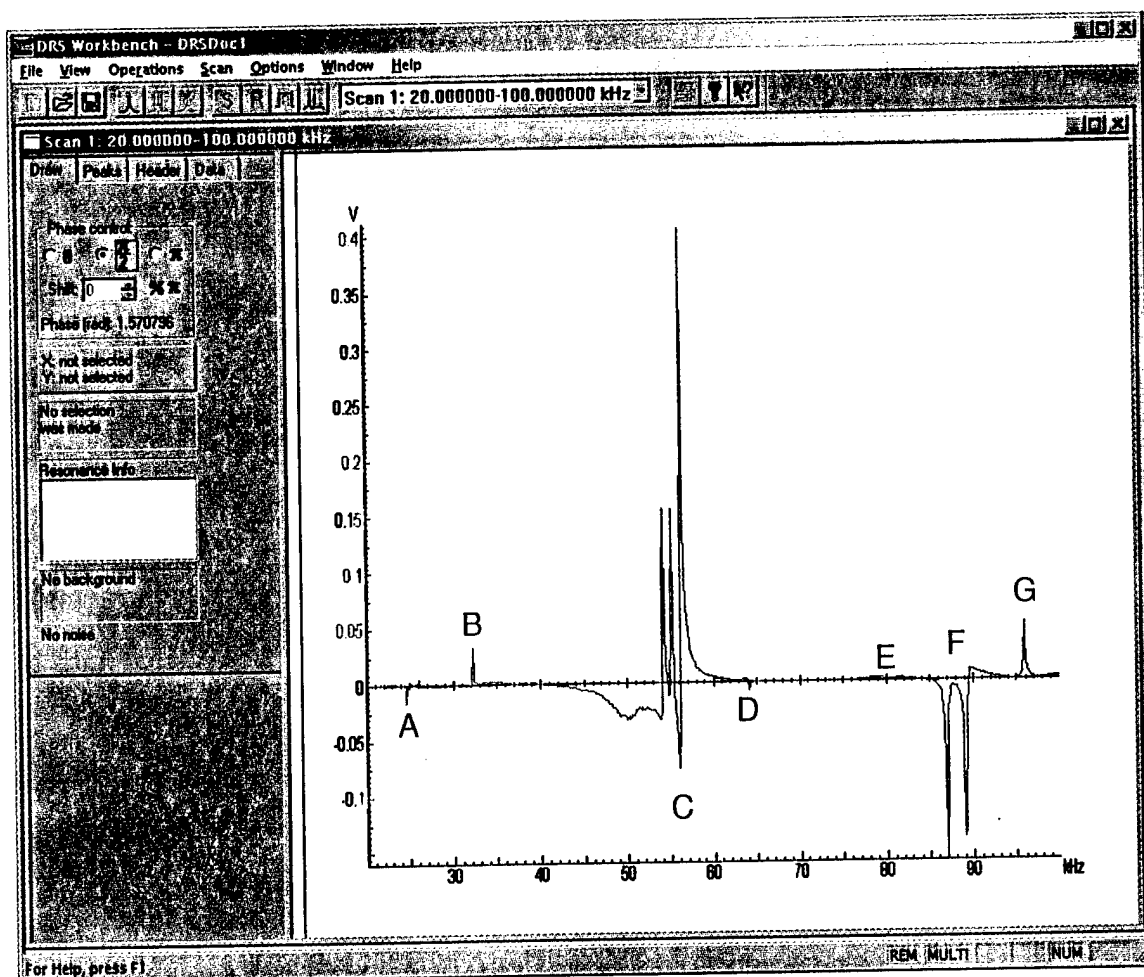


Figure B.4: Initial scan of sample BG-4. Scanned over the range 20 – 100 kHz in order to detect the first ten resonance frequencies seen in Fig. B.3.

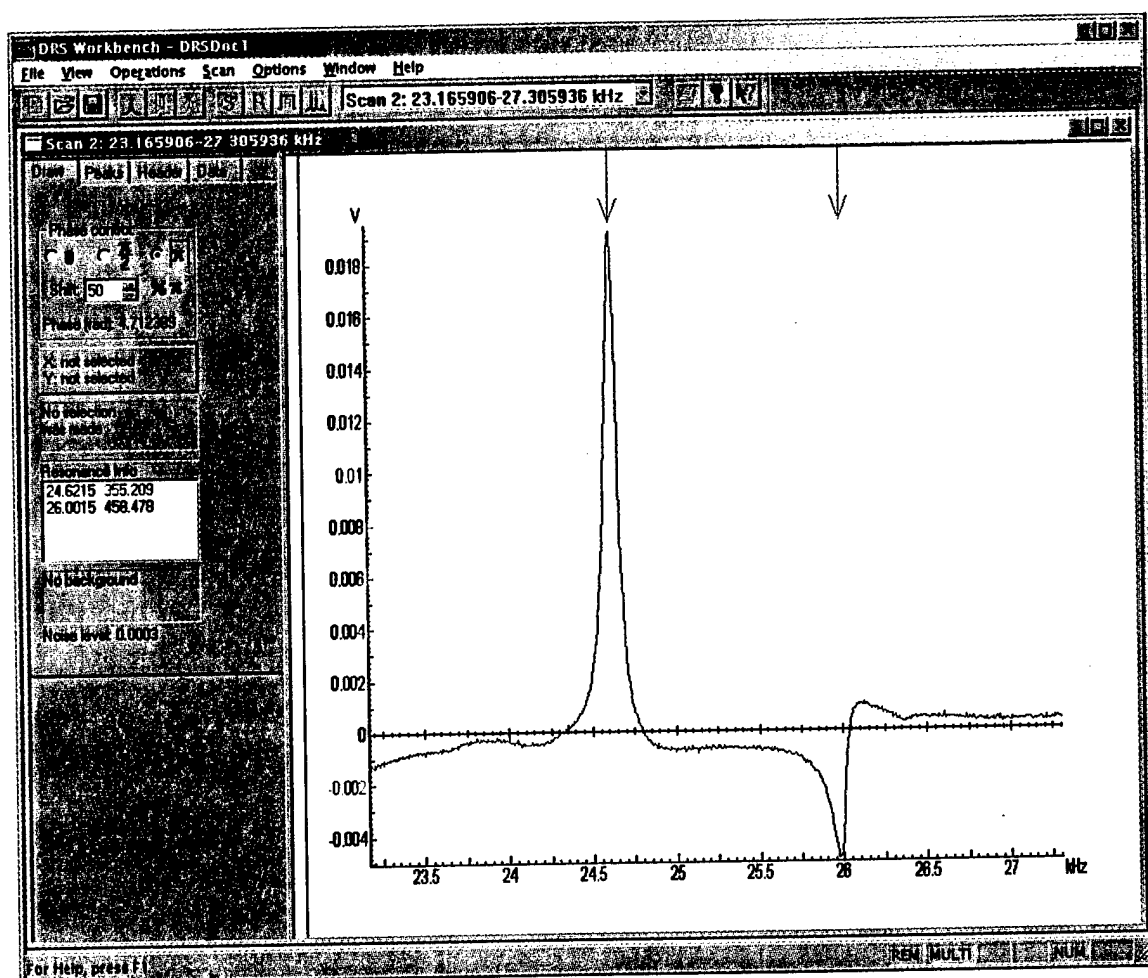


Figure B.5: Scan of region A for sample BG-4. Decreased scanning range to resolve the resonance peak.

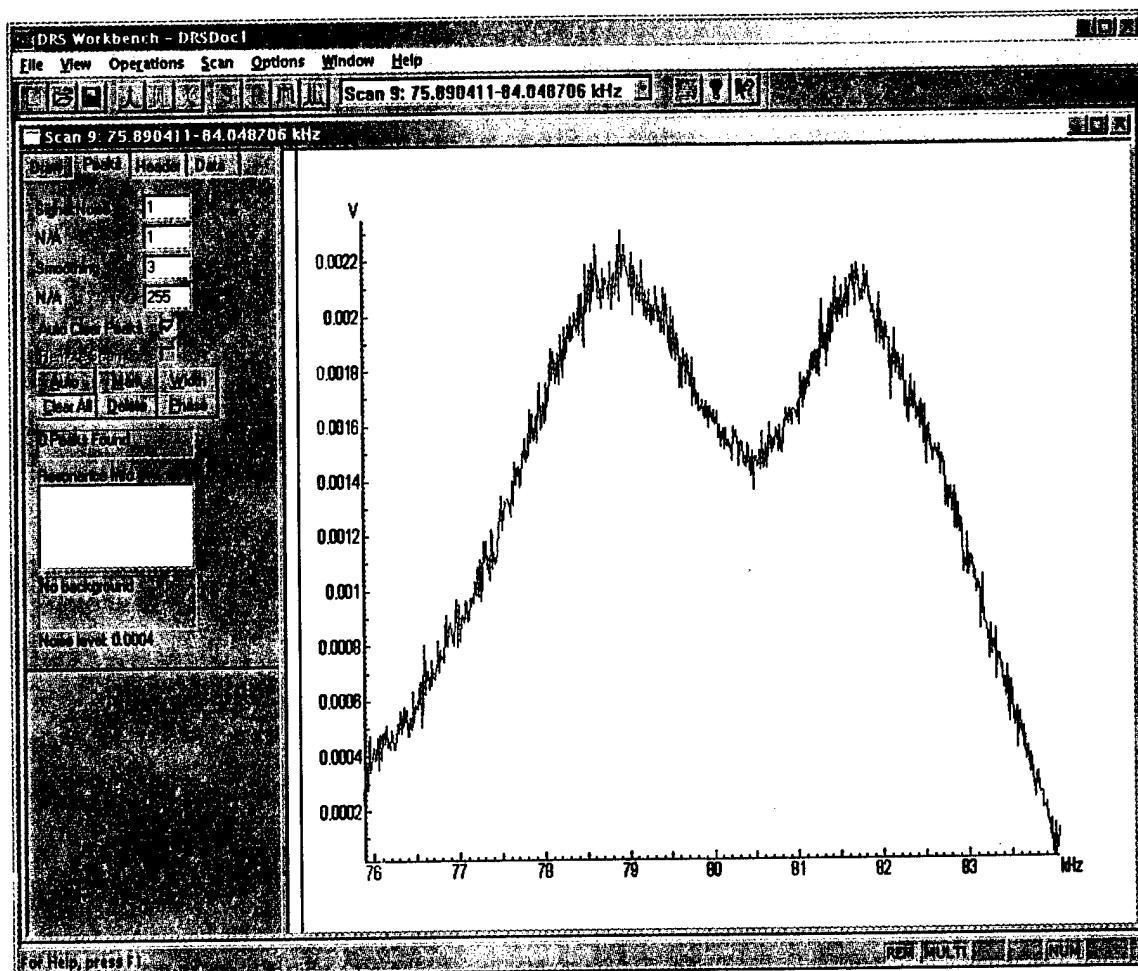


Figure B.6: Artifact scan of sample BG-4, region E. No resonance peaks in this range. Area scanned to illustrate the obvious difference to "peak" shaped artifacts and the actual peaks illustrated in the other scans.

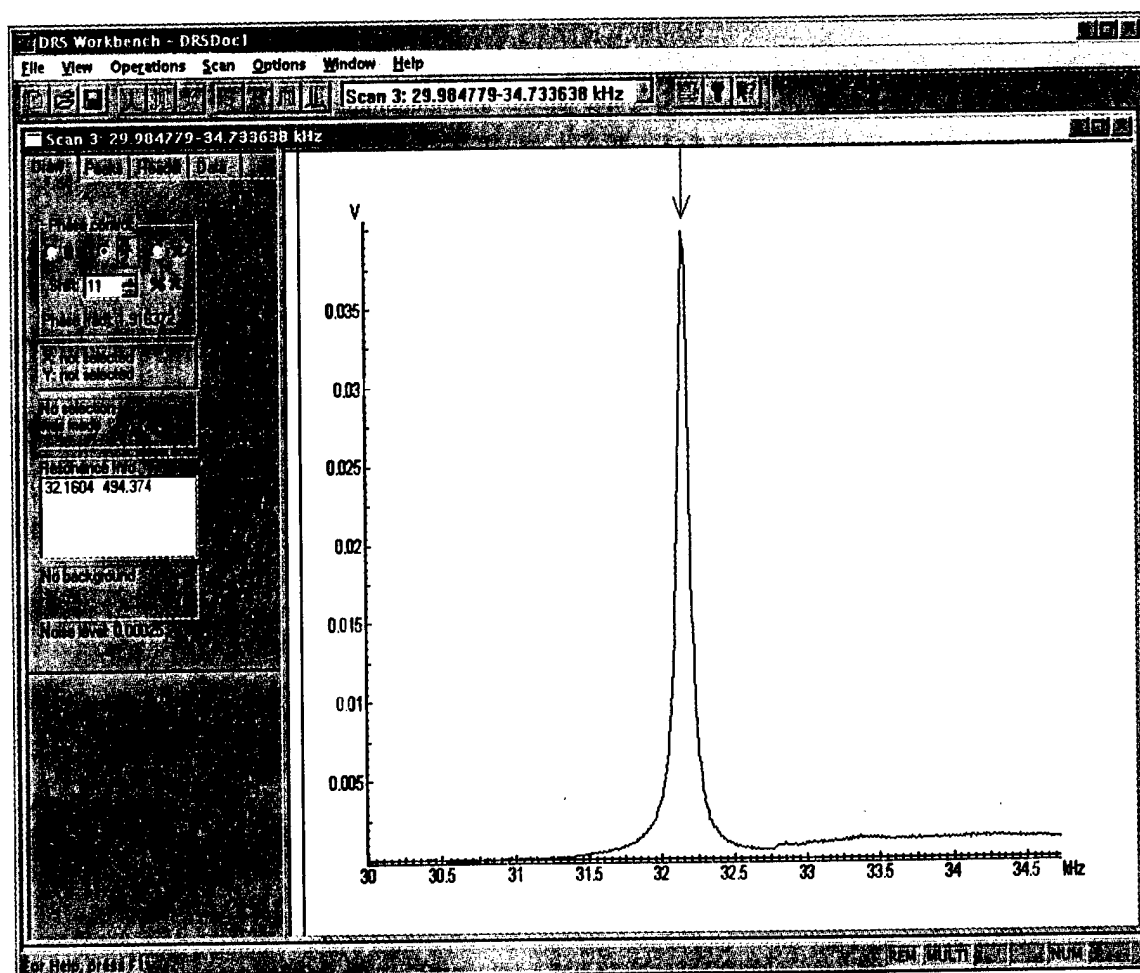


Figure B.7: Sample BG-4, scan of region B.



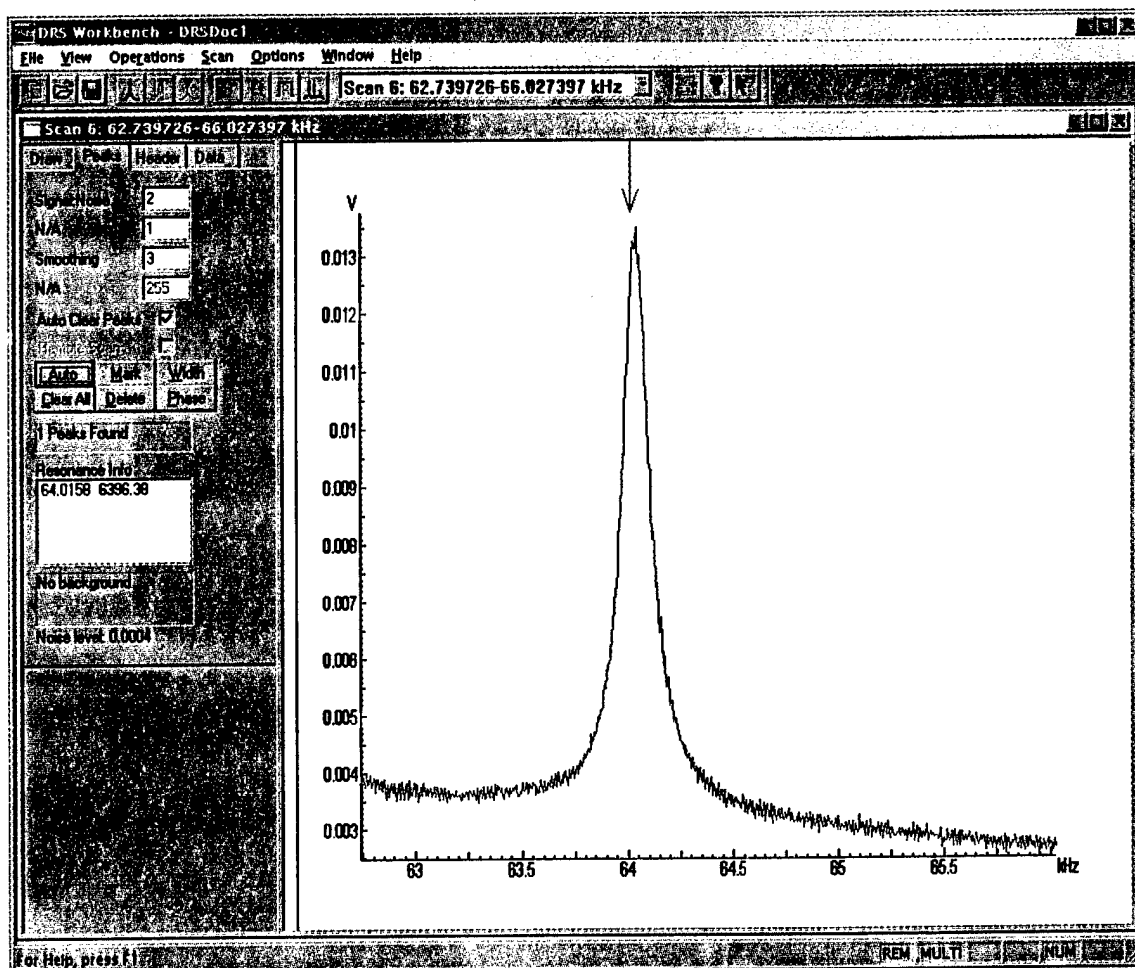


Figure B.9: Sample BG-4, scan of region D.

the first scan (Fig. B.4) there appears to be a small deviation from the background noise just before 80kHz (region E). A closer scan of this area (Fig. B.6) illustrates the difference between a system artifact and resonance. The bumps in region E have a much smaller relative amplitude than the resonances in region A (Fig. B.5), and also have a more amorphous shape than the well-defined peaks in region A. In addition, in subsequent scans, region E changes shape, while resonance frequencies do not. This indicates that there is a weak coupling somewhere in the system, yet it is easily distinguishable from true resonances in the spectrum.

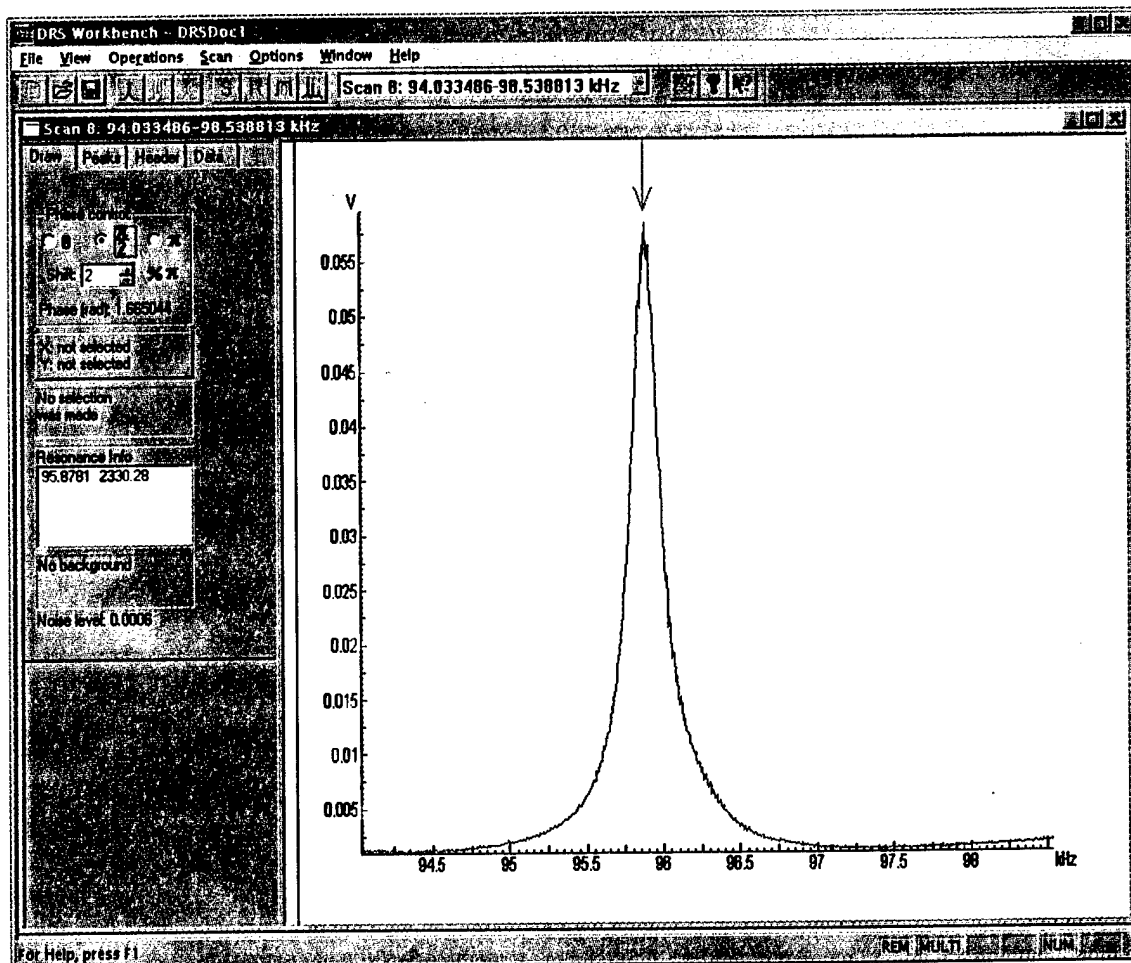


Figure B.10: Sample BG-4, scan of region F.



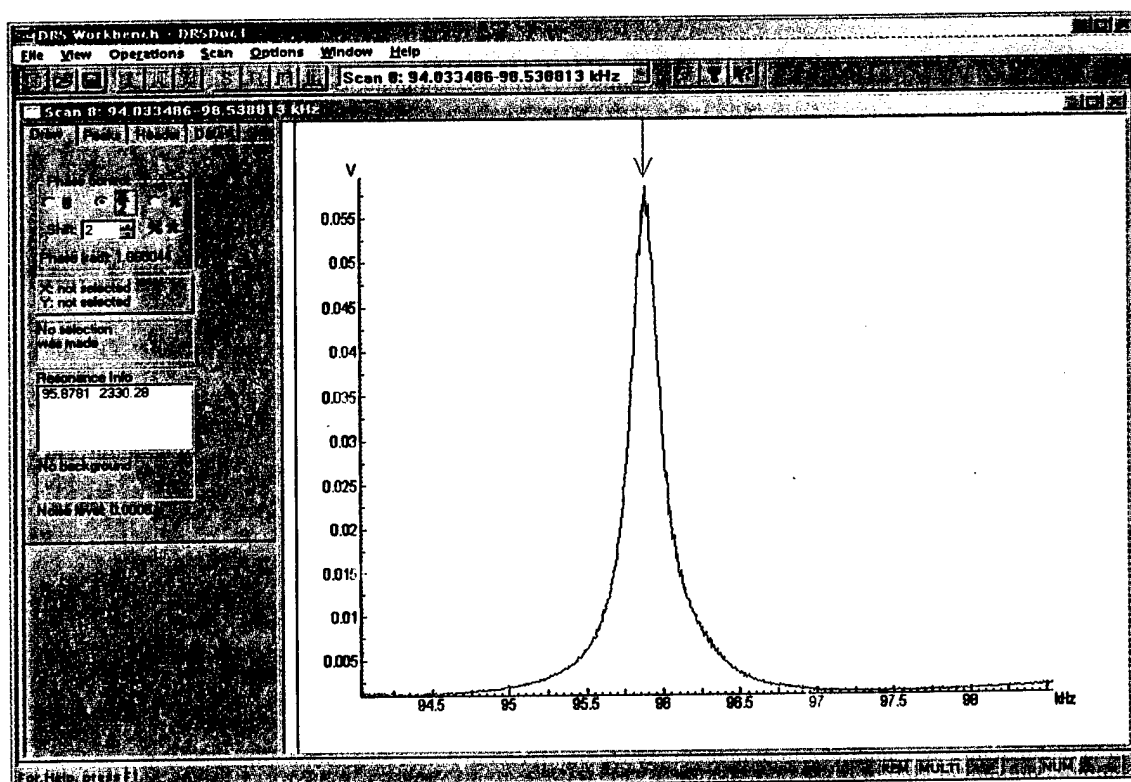


Figure B.11: Sample BG-4, scan of region G.

BG-4

2 3 10 0 26.18 1 1

0.866 0.319

1.29 1.4 5.01

0.024621 0.024762

0.026001 0.028456

0.032160 0.032331

0.054135 0.049300

0.055135 0.053805

0.056274 0.057833

0.064016 0.064169

0.086995 0.085516

0.089145 0.088649

0.095878 0.094112

Sample Name

3rd entry is polynomial solution order

5th entry is sample mass

Initial Guesses for c11 and c44, respectively

Dimensions (order is irrelevant for isotropic)

1.00

1.00

1.00

1.00

1.00

1.00

1.00

1.00

1.00

1.00

1st & 2nd columns are  
experimentally measured frequencies3rd column is a weighting  
parameter for each frequency

Figure B.12: Input file for sample BG-4, containing experimentally measured frequencies from figs. B.4- B.11.

After experimentally measuring the resonance frequencies of our sample, the next step is to run the inversion algorithm [8]. Figure B.12 includes the same sample information as the input file used for the forward calculation (Fig. B.3) with the addition of three columns containing the measured frequencies (columns one and two) and a weighting column indicating the confidence level of the measurement ( $0 \leq \text{weighting value} \leq 1$ ). The final output is shown in Fig. B.13. The information provided in the output file includes the measured resonance frequencies, expected resonance frequencies, the difference between them (fex, fr, %err columns), the bulk modulus (an engineering constant), individual moduli, and the accuracy of the final solution (rms error).

BG-4

free moduli are c11, c44

free dimensions are d1, d2, d3

using 10 order polynomials mass= 26.1800 gm rho= 2.893 gm/cc

n	fex	fr	%err	wt	k	i	df/d(moduli)
1	0.024621	0.024533	-0.36	1.	1	2	0.28 0.72
2	0.026001	0.025976	-0.10	1.	7	2	0.28 0.72
3	0.032160	0.032055	-0.33	1.	4	1	0.00 1.00
4	0.054135	0.054361	0.42	1.	2	2	0.23 0.77
5	0.055135	0.055040	-0.17	1.	5	1	0.29 0.71
6	0.056274	0.056326	0.09	1.	8	2	0.22 0.78
7	0.064016	0.064057	0.06	1.	3	2	0.00 1.00
8	0.086995	0.087226	0.27	1.	1	3	0.19 0.81
9	0.089145	0.089194	0.05	1.	7	3	0.18 0.82
10	0.095878	0.095932	0.06	1.	4	2	0.00 1.00

Bulk Modulus= 0.573

c11	c22	c33	c23	c13	c12	c44	c55	c66
1.0444	1.0444	1.0444	0.3370	0.3370	0.3370	0.3537	0.3537	0.3537

d1	d2	d3
1.29241	1.40270	4.99105

loop#10 rms error= 0.2319 %, changed by -0.0000063 %

length of gradient vector= 0.194379 blamb= 0.000000

eigenvalues	eigenvectors
0.02097	0.97 0.25-0.04-0.06 0.00
0.81465	0.05-0.43 0.00-0.90 0.00
2.66530	-0.03 0.20 0.65-0.10-0.72
34.43162	-0.04 0.02-0.75-0.01-0.67
9827496.70739	0.24-0.85 0.13 0.41-0.19

chisquare increased 2% by the following % changes in independent parameters

0.94	0.15	-0.05	-0.05	0.10
0.04	-0.20	0.05	0.00	-0.06
0.00	0.00	0.09	-0.10	0.00

Figure B.13: Final output file for sample BG-4.

## REFERENCES

1. J. Maynard, Resonant ultrasound spectroscopy, *Phys Today* vol. 49 (1), 26-31 Jan 1996
2. J. L. Sarrao, S. R. Chen, W. M. Visscher, Ming Lei, U. F. Kocks and A. Migliori, Determination of the Crystallographic Orientation of a Single Crystal using Resonant Ultrasound Spectroscopy, *Rev. Sci. Inst.* vol. 65 (6), 2139-40, 1994.
3. H. Oda, O. L. Anderson, D. G. Isaak, and I. Suzuki, Measurement of elastic properties of single-crystal CaO up to 1200K, *Phys.Chem. Miner.*, 19, 96, 1992.
4. J. L. Sarrao, D. Mandrus, A. Migliori, Z. Fisk, I. Tanaka, H. Kojima, P.C. Canfield, and P.D. Kodali, Complete elastic moduli of  $\text{La}_{2-x}\text{Sr}_x\text{CuO}_4$  ( $x = 0.00$  and  $0.14$ ) near the tetragonal-orthorhombic structural phase transition, *Phys. Rev. B*, 18, 50, 1994.
5. A. Migliori, and J. L. Sarrao, *Resonant Ultrasound Spectroscopy*, John Wiley & Sons, Inc., 1997.
6. F. Birch, "Compressibility; Elastic Constants", *Handbook of Physical Constants*, Geological Society Memoir 97, 97-106, 1966.

7. T. Bourbie, O. Coussy, B. Zinszner, *Acoustics of Porous Media*, Gulf Pub. Co. 1987.
8. DRS Workbench and analyzing software, Dynamic Resonance Systems, Inc., 1999
9. W. M. Visscher, A. Migliori, T. M. Bell, R. A. Reinert, On the Normal Modes of Free Vibration of Inhomogeneous and Anisotropic Elastic Objects, *J. Acoust. Soc. Am.* 90 (4), 2154, 1991.
10. V. Kari, Univ. of Nevada, Reno, 2000.
11. J. D. Achenbach, *Wave Propagation in Elastic Solids*, Elsevier Science Publishing Company, Inc., 1984.
12. T.W. Darling and A. Migliori, "Global symmetry, the phonon density of states and RUS," Proceedings of the Resonance Meeting, May 30-June 1, 1999, Volume 1, pgs 96-106, NCPA Report LF0400-01.
13. W. H. Press, S. A. Teukolsky, W. T. Vetterling, B. P. Flannery, *Numerical Recipes in FORTRAN The Art of Scientific Computing*, Cambridge University Press, 1992.
14. K. Lau and A. K. McCurdy, Elastic anisotropy factors for orthorhombic, tetragonal, and hexagonal crystals, *Phys. Rev. B*, 58, 8980, 1998.
15. R. S. Carmichael, *Handbook of Physical Properties of Rocks*, CRC Press, 1982.

16. A. L. Fetter, J. D. Walecka, *Theoretical Mechanics of Particles and Continua*, McGraw-Hill, Inc., 1980.